Co-solvent Engineering for Improved Stability of the $Ti_3C_2T_x$ Zn-free Anode

Name: Zerui Wang
Project duration: November 1st, 2023 – July 29th, 2024
Supervisor: Prof. Xuehang Wang, Prof. Yaiza Gonzalez Garcia
Daily supervisor: Chaofan Chen

TU Delft

Abstract

With the depletion of energy resources and escalating environmental issues, the development of new energy sources and advanced energy storage devices has become increasingly critical. Zinc-ion batteries have attracted significant attention due to their lower cost and safer chemistry. A major focus of zinc-ion battery research is the development of zinc anodes and electrolyte design. Zinc-free anodes have emerged as a promising strategy, offering higher zinc utilization compared to traditional zinc metal anodes (approximately 10%). Among many zinc-free anodes, $Ti_3C_2T_x$, a MXene (transition metal nitride/carbide layered material), stands out due to its lower lattice mismatch (~10%), higher conductivity, superior mechanical properties, and good hydrophilicity. However, the higher zinc utilization of zinc-free anodes presents challenges for the stable plating/stripping of zinc. Co-solvent engineering is a convenient and direct approach to improving the stability of zinc-free anodes.

In this study, we propose the use of PEG and IPA as co-solvents added to a 1M $Zn(OTF)_2$-H_2O electrolyte to enhance the stability of $Ti_3C_2T_x$ zinc-free anodes. We found that the addition of PEG reduced the hydrogen evolution current by 0.42 mA (at -1.3 V vs. Ag wire), indicating suppression of the hydrogen evolution reaction. Furthermore, the addition of PEG in the electrolyte inhibits the 2D diffusion of zinc on the Ti_3C_2 surface and promotes zinc deposition along the (002) crystal direction, increasing the (002)/(001) ratio from 0.59 to 0.86, leading to more uniform zinc deposition. Consequently, the Ti_3C_2 zinc-free anode achieved a coulombic efficiency of 97.67% and a cycle life of 268 hours. Similarly, the addition of IPA reduced the hydrogen evolution current by 0.39 mA (at -1.3 V vs. Ag wire), indicating a weaker hydrogen evolution reaction. Moreover, the addition of IPA in the electrolyte inhibits 2D diffusion on the Ti_3C_2 surface and facilitates zinc deposition along the (002) crystal direction, increasing the (002)/(001) ratio from 0.59 to 0.87. The formation of an SEI containing $ZnCO_3$, ZnFx, and F-rich organics helps to homogenize the Zn ion gradient. Ultimately, the Ti_3C_2 zinc-free anode achieved a high coulombic efficiency of 98.95% and a cycle life of over 1200 hours in the IPA-containing electrolyte.

Co-solvent Engineering for Improved Stability of the $Ti_3C_2T_x$ Zn-free Anode

TU Delft

Content

Abbreviations **4**

1 Background **6**
1.1 Zn anode 8
1.1.1 Mechanism of Zinc deposition 8
1.1.2 Challenges of Zinc anode 11
1.2 Zn-free anode 13
1.3 MXene 14
1.3.1 Composition and structure of MXene 14
1.3.2 Synthesis of MXene 15
1.3.3 Ti_3C_2 Zn-free anode 18
1.4 Co-solvent Engineering 18
1.4.1 Breaking the hydrogen bond network 18
1.4.2 Adjusting the solvation structure 19
1.4.3 Adsorption 21
1.5 Scope of Research 21

2 Experimental **23**
2.1 Material synthesis 23
2.1.1 Synthesis of Ti_3C_2 23
2.1.2 Preparation of electrolyte 23
2.1.3 Cell Assembly 23
2.2 Material characterization 23
2.2.1 Fourier-transform infrared spectroscopy (FTIR) 23
2.2.2 X-ray diffraction (XRD) 24
2.2.3 Scanning Electron Microscopy (SEM) 24
2.2.4 X-ray photoelectron spectroscopy (XPS) 25
2.3 Electrochemical characterization 26
2.3.1 Galvanostatic Charge and Discharge (GCD) 26
2.3.2 Electrochemical Impedance Spectroscopy (EIS) 27
2.3.3 linear sweep voltammetry (LSV) 28
2.3.4 Cyclic Voltammetry (CV) 28
2.3.5 Chronoamperometry (CA) 29

3 PEG co-solvent for improved stability of the Ti_3C_2 Zinc-free anode **30**
3.1 Inhibition of hydrogen evolution 30
3.2 Deposition behavior 32
3.2.1 Deposition of zinc on Ti_3C_2 surface 32
3.2.2 Overall morphology and texture of zinc deposited on $\mathbf{Ti_3C_2}$ surface 35
3.3 Electrochemical Performance of Ti_3C_2 Zn-free anode 38

4 Weakly solvating Zn-based aqueous electrolyte enabled by IPA cosolvent **40**
4.1 Formation of weak solvation structure 40

4.2 Bulk electrolyte properties 42
4.3 Deposition behavior 43
4.3.1 Deposition of zinc on Ti_3C_2 surface 43
4.3.2 Overall morphology and texture of zinc deposited on $\mathbf{Ti_3C_2}$ surface 46
4.4 Formation of SEI 48
4.5 Electrochemical Performance of Ti_3C_2 Zn-free anode 51

5 Discussion and Conclusion 53
5.1 PEG and IPA co-solvent improves the stability of Ti_3C_2 zinc-free anode 53
5.2 The role of PEG and IPA in improving the zinc-free Ti_3C_2 anode 53
5.3 The compromise between weak solvation and breaking hydrogen bond network 55
5.4 The importance of solvent conductivity 55

6 Recommendations 56

Appendix 58
Extended Results 58

Reference 61

Abbreviations

Abbreviations	Definition
PEG	Polyethylene glycol
IPA	Isopropanol
BFT model	Bewick, Fleischman, and Thirsk model
SH model	Scharifker–Hills model
AFT model	Armstrong, Fleischmann and Thirsk model
ZIB	Zinc ion battery
HER	Hydrogen evolution reaction
PC	Polycarbonate
SHE	Standard hydrogen electrode
SEI	Solid-electrolyte interphase
DFT	Density functional theory
DGM	Diglyme
TMU	Tetramethylurea
DN	Donor number
DMSO	Dimethyl sulfoxide
SSIP	Solvent-separated ion pair
CIP	Contact Ion pair
MD	Molecular dynamics
FTIR	Fourier-transform infrared spectroscopy
XRD	X-ray diffraction
SEM	Scanning electron microscope
XPS	X-ray photoelectron spectroscopy
GCD	Galvanostatic charge and discharge
EIS	Electrochemical impedance spectroscopy
LSV	Linear sweep voltammetry
CV	Cyclic voltammetry

CA	Chronoamperometry
APS	Ammonium persulfate
CVD	Chemical vapor deposition
E_{λ}	Switching potential
E_{co}	Crossover potential
DMC	Dimethyl carbonate
DME	1,2-dimethoxyethane
DMF	N, N-dimethylformamide
DMA	N, N-dimethyl acetamide
XANES	X-ray absorption near-edge structure
Ft-EXAFS	Fourier transformed extended X-ray absorption fine structure
HCP	hexagonal closed packed

1 Background

While renewable energy sources are growing rapidly, the substantial reliance on weather, temperature, and geographic location for renewable energy production still results in a mismatch between power generation and demand. This mismatch can even impact the stability and operation of the power grid [1]. Hence, energy storage devices are essential to alleviate the intermittency of renewable energy sources. With the surge in electric vehicle development, lithium-ion batteries have emerged as the dominant choice for energy storage, offering high energy and power density[2].

However, the development of lithium-ion batteries is constrained by factors such as limited lithium resources, safety concerns, and cost issues. Therefore, the emerging zinc-ion battery (ZIS) has received widespread attention from researchers due to the safety, abundance and affordability (2 US$/kg vs lithium metal 19 US$/kg) (figure 1).[3] Another potential benefit is that aqueous electrolytes can be used due to the stable chemistry, which also brings better conductivity (1 mS/cm^{-2}) to zinc-ion battery electrolytes.[4]

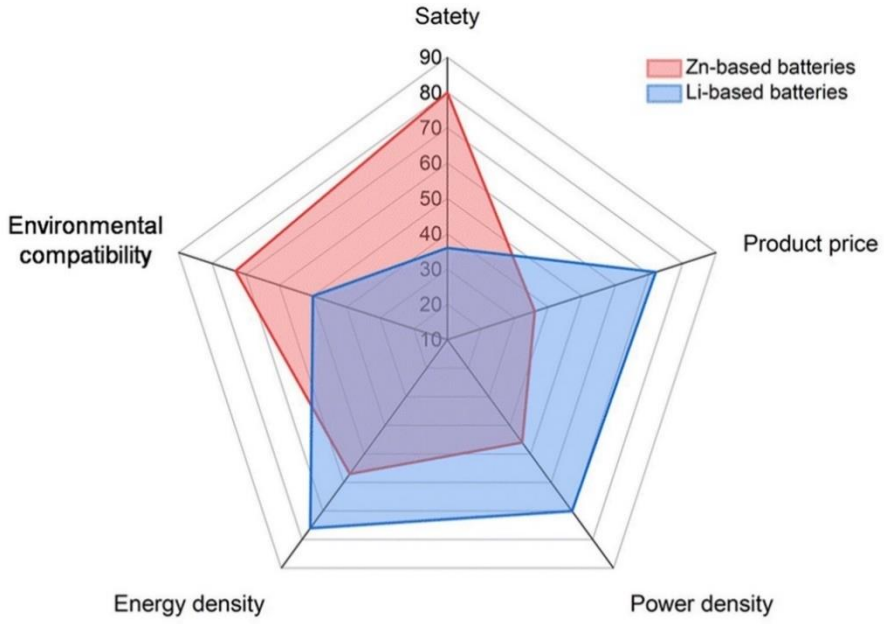

Figure 1 Comparison of Zn-based batteries and Li-based batteries from multiple metrics[4]

The structure of a zinc-ion battery is similar to that of a lithium-ion battery, consisting of an anode, a cathode, a separator, and electrolyte. Binders and conductive agents are sometimes introduced into the electrodes to enhance performance. The voltage produced by the battery arises from the electrochemical potential difference between the cathode and the anode. The separator in the battery isolates the cathode and anode to prevent short circuits, while the electrolyte facilitates charge transport within the battery through the conduction of anions and cations. In a general context, cathode materials typically exhibit a layered structure, enabling the storage of charges by inserting and extracting zinc ions. Common ZIS cathodes include manganese-based materials, vanadium-based materials, Prussian blue analogues, etc. [5], [6], [7] Research on anode materials currently focuses on Zinc

metal[8]. This research will primarily concentrate on electrolyte for zinc metal anodes. In Section 1.1, we will discuss in detail the working principles and the challenges associated with zinc metal anodes.

Although zinc-ion batteries have many advantages, their energy density and power density still fall short compared to lithium-ion batteries (figure.1). This highlights the direction and scope for future research improvements: (1) Developing electrode materials with higher specific capacity, especially zinc metal anodes and more suitable cathodes, and (2) Developing proper electrode and electrolyte systems for high-power and high energy density energy storage systems.

1.1 Zn anode

As previously mentioned, enhancing energy density is crucial for the practical application of zinc-ion batteries, and the zinc anode fulfills this requirement. It has high specific capacity (840 mAh g^{-1}), volumetric capacity (5850 mAh cm^{-3}), and negative potential (-0.76 V). Additionally, it is also affordable, non-flammable, and stable in air. These characteristics make the zinc anode a key focus in the research and development of zinc-ion batteries. In this chapter, the deposition mechanism and challenges of zinc anode will be explained.

1.1.1 Mechanism of Zinc deposition

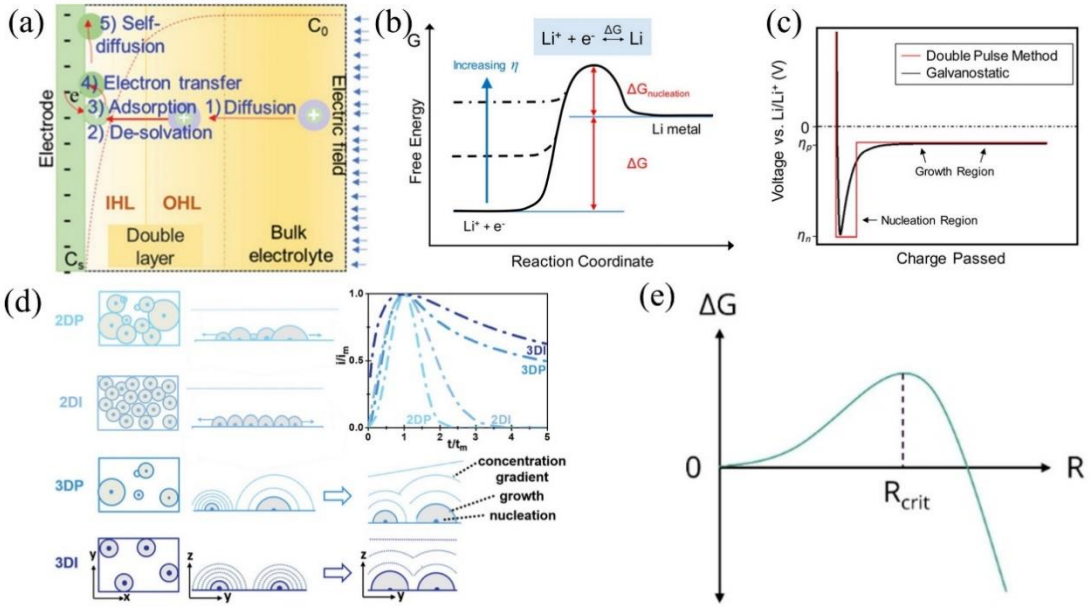

Figure 2 (a) Illustrations of Zn deposition process[9] (b) Changes of free energy and (c) typical voltage curve at the Zn deposition process.[10] (d) Schematic illustration of 2DP/2DI (BFT models) and 3DP/3DI (SH models) (x–y is parallel to the substrate; y–z is vertical to the substrate[11] (e) Impact of radius on change in Gibbs free energy, Rcrit marks the peak and the critical nucleus radius.[12]

The working principle of a zinc anode involves the plating and stripping of zinc metal. Therefore, thoroughly understanding the deposition process is crucial for enhancing zinc anodes. From the perspective of zinc ions, the deposition process can be divided into five steps (as shown in Figure 2(a)) (1) Solvated zinc ions diffuse from the cathode side to the anode side under the influence of the electric field. (2) When the solvated zinc ions approach the inner Helmholtz layer, desolvation occurs, causing the zinc ions to lose the surrounding polar molecules and anions. (3) The desolvated zinc ions are adsorbed onto the electrode surface to charge the double layer and (4) simultaneously get electrons, being reduced to zinc metal. (5) Finally, the zinc metal on the surface may undergo 2D diffusion to find the most energetically favorable site.[9]

The kinetics of the above five steps are quite different. Typically, the charge transfer step is faster than the zinc ion diffusion step, resulting in a difference in zinc ion concentration between the interface and

the bulk electrolyte. This strong concentration polarization will accelerate the dendrite growth of the electrode. Enhancing the zinc ion flux is an effective way to reduce polarization. The Nernst-Planck equation is used to describe the ion diffusion flux at the anode interface:[13]

$$J = -\frac{zecD}{KT}\frac{dV}{dx} - D\left(\frac{dc}{dx}\right) + cv_x \quad (1)$$

Where z, e, c, D, K, V, x, v_x are the charge number, the unit charge, the ion concentration, the diffusion coefficient, the Boltzmann constant, the electric potential, the distance to electrode, and the convective velocity, respectively. From the above formula, it can be concluded that increasing the diffusion coefficient, enhancing the electric field, increasing the concentration and strengthening the convection are all ways to enhance the diffusion step and alleviate polarization.

From the perspective of macroscopic anode, the deposition of zinc can be primarily divided into two steps: initial nucleation and subsequent growth[14]. Initial nucleation is the first step in zinc deposition. As shown in Figure 2 (b), the generation of new zinc metal phase by zinc ions must overcome the energy barrier of forming a critical cluster of atoms, resulting in a nucleation overpotential.[10]. (Figure 2 (c)) The initial nucleation process mainly controls the number and density of nucleation sites. In the subsequent growth step, where a different overpotential is shown, Zn ions will preferentially deposit at these nucleation sites rather than evenly across the entire zinc metal surface.[15]

Specifically, since the surface of zinc metal is not absolutely smooth, different surface free energies will promote the formation of uneven zinc nuclei. Under constant voltage conditions, the density of nuclei (N) can be described by the following equation:[11]

$$N = N_0[1 - \exp(-At)] \quad (2)$$

Where N_0 is density of available nucleation site, A is nucleation rate.

From the above equation, when the nucleation rate is high (A>>1/t), the nucleation sites will be exhausted quickly, thus forming nuclei with similar size and high density within a fixed time t. This process is called “instantaneous nucleation”. On the contrary, when the nucleation rate is low, the density of the nuclei will increase linearly with time, resulting in uneven nuclei radius and low density, so-called “progressive nucleation”. (figure 2 (d)) Since the nucleation rate A is dependent on the overpotential, we can adjust the nucleation process by tuning the overpotential. The subsequent growth process can be divided into a 2D diffusion step dominated by the surface diffusion of adsorbed atoms and a 3D diffusion step dominated by the diffusion of zinc in the electrolyte..[11]

The above nucleation and growth processes can be described by 2 commonly used models. (as shown in Figure 2 (d)) The first is the 2D diffusion model determined by Bewick, Fleischman, and Thirsk (BFT), including: (1) 2D progressive nucleation and (2) 2D instantaneous nucleation:[11], [16]

2D progressive nucleation:

$$\frac{j}{j_m} = \left(\frac{t}{t_m}\right)^2 \left\{\exp\left[-2\frac{(t^3 - {t_m}^3)}{3{t_m}^3}\right]\right\} \quad (3)$$

2D instantaneous nucleation:

$$\frac{j}{j_m} = \left(\frac{t}{t_m}\right)\left\{\exp\left[\frac{t^2 - {t_m}^2}{2{t_m}^2}\right]\right\} \quad (4)$$

Where j_m and t_m are the maximum values of current and corresponding time respectively.

The second is the 3D diffusion model determined by Scharifker–Hills (SH), including (3) 3D progressive nucleation and (4) 3D instantaneous nucleation:[11], [17]

3D progressive nucleation:

$$\frac{j}{j_m} = \left(\frac{1.9542}{\frac{t}{t_m}}\right)^{\frac{1}{2}}\left\{1 - \exp\left[1.2564\frac{t}{t_m}\right]\right\} \quad (5)$$

3D instantaneous nucleation:

$$\frac{j}{j_m} = \left(\frac{1.2254}{\frac{t}{t_m}}\right)^{\frac{1}{2}}\left\{1 - \exp\left[2.3367\left(\frac{t}{t_m}\right)^2\right]\right\} \quad (6)$$

Where j_m and t_m are the maximum values of current and corresponding time respectively.

In addition to the above four models, there is a 3D diffusion model based on conical deposition proposed by Armstrong, Fleischmann and Thirsk (AFT) that is closer to the test of zinc metal. [18]The previous four models will always reach 0 mA in a certain period. In the AFT model, the current will eventually maintain a constant value, which is more similar to the chronoamperometry observed in the literature.[19], [20] According to the AFT model, the current-time relationship is as follows:

$$J_{3DP} = nFk_{2g}\left[1 - \exp\left[-\frac{\pi M^2 A N_0 {k_{1g}}^2 t^3}{3\rho^3}\right]\right] \quad (7)$$

With the value of the steady-state current is given by

$$J_m = \frac{nFk_{2g}}{4} \quad (8)$$

Where M is molar mass, N_0 is density of available nucleation site, A is nucleation rate, k_{1g} is the lateral growth rate constant of nuclei, ρ is the density of deposition material.

The models mentioned above are all suitable for constant voltage deposition, while constant current deposition is more frequently used during the battery cycle. Unfortunately, a widely verified and accepted constant current electrodeposition model does not exist. Thus, the explanation provided here focuses on uncovering the types of nucleation and growth, as well as the potential for enhancing electrodeposition. The development of a precise quantitative model for constant current remains an urgent task for researchers.

The radius/size of the nucleus is also a point of concern during nucleation and growth. According to the classical theory of homogeneous nucleation, the initial nucleation needs to overcome the nucleation energy barrier (shown in Figure 2 (e)):[10]

$$\Delta G_{nucleation} = -\frac{4}{3}\pi r^3 \Delta G_V + 4\pi r^2 \gamma \tag{9}$$

Where ΔG_V is the free energy change per volume, γ is the surface energy of Zn-electrolyte interface. The relationship between ΔG_V and overpotential (η) is:

$$\Delta G_V = \frac{\mathrm{F}|\eta|}{V_m} \tag{10}$$

Where F is Faraday's constant, V_m is molar volume of Zinc. According to the principle of minimum free energy, the critical size can be obtained (shown in Figure 2 (e)):

$$r_{critical} = \frac{2\gamma V_m}{F|\eta|} \tag{11}$$

Through the above discussion, Zn deposition is a complex process. The steps and key parameters of Zn deposition are analyzed from the perspective of microscopic zinc ions and macroscopic nucleation and growth theory, thus laying a foundation for the understanding of zinc anode.

1.1.2 Challenges of Zinc anode

After explaining the advantages and mechanisms of zinc anode in detail, there are still many challenges that need to be solved. The challenges faced by zinc anodes can be roughly divided into three issues: dendrite growth, hydrogen evolution, and side reactions.

Like all metal anodes, zinc anodes also experience severe dendrite problems. Although zinc metal dendrites do not cause serious combustion and explosion problems due to its special aqueous electrolyte and stable zinc chemistry, the generation of zinc dendrites still causes influence the stability and cycle life of ZIB.

As mentioned in 1.1.1 above, the subsequent growth steps of zinc metal are not uniformly deposited on the surface of the zinc substrate but tend to be deposited on the preferred zinc nucleation site, leading to dendrite growth. This is mainly due to the following reasons: (1) From a thermodynamic point of view, the tip of the zinc nucleus protrusion has a higher curvature and accumulates a higher charge density, thereby attracting more zinc ions to deposit on the tip, which is also called the "tip effect"(figure 3 (a)).[21], [22], [23] (2) From a kinetic perspective, since the charge transfer step of zinc ions mentioned in 1.1.1 is usually faster than the diffusion step, the deposition of zinc is controlled by diffusion and produces a concentration difference. This process is affected by the diffusion equation and the Nernst-Planck equation (equation (1))[13]. When the current is large enough, the salt concentration on the electrode surface will drop to zero, resulting in severe dendrite growth. The time when the salt

concentration on the electrode surface drops to zero is called the "Sand's time" and is described by the following formula:[24], [25]

$$t_{sand} = \pi D_{app} \frac{(z_c c_0 F)^2}{4(J t_a)^2} \quad (12)$$

where t_{sand} is Sand's time, z_c is the charge number of the metal cation, c_0 is the bulk salt concentration, F is Faraday's constant, J is the current density, and t_a is the transference number of anions.

In addition, dendritic growth is influenced by the mode of 2D/3D diffusion. As discussed earlier in chapter 1.1.1, zinc nucleation under 2D diffusion control primarily occurs through the migration of adsorbed zinc particles adsorbed on the Zn metal surface to sites of lower energy. Consequently, dendrites, which have higher surface energy, tend to grow more rapidly. Conversely, growth under 3D diffusion control is constrained by the concentration gradient and solubility of zinc particles in the solution, promoting a more uniform growth morphology.[11]

As the battery cycles, the growth of zinc dendrites will eventually penetrate the separator and form a short circuit, causing battery failure. Therefore, understanding and alleviating the growth of dendrites is important for improving the coulombic efficiency and cycle life of zinc anodes.

In addition to dendrite formation, the hydrogen evolution reaction (HER) caused by aqueous electrolyte will also affect the performance of zinc anode.

Under neutral conditions, the deposition of zinc metal and the hydrogen evolution reaction are as follows:

$$Zn \leftrightarrow Zn^{2+} + 2e^- (E_0 = -0.76\ V\ vs.SHE) \quad (13)$$

$$2H^+ + 2e^- \rightarrow H_2 (E_0 = 0\ V\ vs.SHE) \quad (14)$$

As the competitive process of zinc deposition, the hydrogen evolution reaction will occur before the zinc deposition process due to the higher redox potential. However, Zn deposition in aqueous electrolytes is still feasible even though HER may occur. This can be described by the Tafel equation:[26]

$$\eta = b\ logi + a \quad (15)$$

Where η is the hydrogen evolution overpotential, i is the current density, b is the Tafel slope constant, and the constant a is the overpotential when the current density i is equal to the unit current density. For most metals, b is similar (about 0.12 V). Therefore, the intercept a almost determines the hydrogen evolution overpotential on Metal surface. Zinc has a high constant a (about 1.24 V), which can lower the actual HER potential to a certain extent.[27], [28]

The hydrogen evolution reaction can also have a serious impact on the battery. First, excess hydrogen in a sealed battery may increase the internal pressure and cause battery damage. Second, competitive hydrogen evolution will hinder the electrolyte/electrode contact and reduce coulombic efficiency.[15] Furthermore, hydrogen evolution will also cause the pH value of the electrolyte to increase, resulting in serious side reactions.

The side reactions mainly come from dissolved oxygen and the gradually increasing pH of the electrolyte. Some reports indicate that dissolved oxygen may cause corrosion of zinc anodes:[29]

$$2Zn + O_2 + 2H_2O \rightarrow 2Zn(OH)_2 \quad (16)$$

As the cycle progresses, HER consumes a large amount of hydrogen ions, resulting in the accumulation of hydroxide. This causes the hydroxide ions to react with zinc ions as a side reaction. However, the byproducts may vary depending on the anion, for example, in the common $ZnSO_4$ salt, the following reaction may occur:[30]

$$4Zn + 6OH^- + {SO_4}^{2-} + xH_2O = ZnSO_4(OH)_6 \cdot xH_2O \quad (17)$$

Different byproducts were observed in different zinc salts, such as $(Zn(CF_3SO_3)_a(OH)_b \cdot xH_2O$ in $Zn(OTF)_2$ [31]and $Zn_4ClO_4(OH)_7$ in $Zn(ClO_4)_2$ [32]. Unfortunately, unlike the traditional solid electrolyte interface (SEI), this layer of byproducts cannot conduct ions [30] [31] [32]. This means that as the byproducts accumulate, the electrode interface will gradually become insulated, leading to greater polarization and more severe dendrite growth.

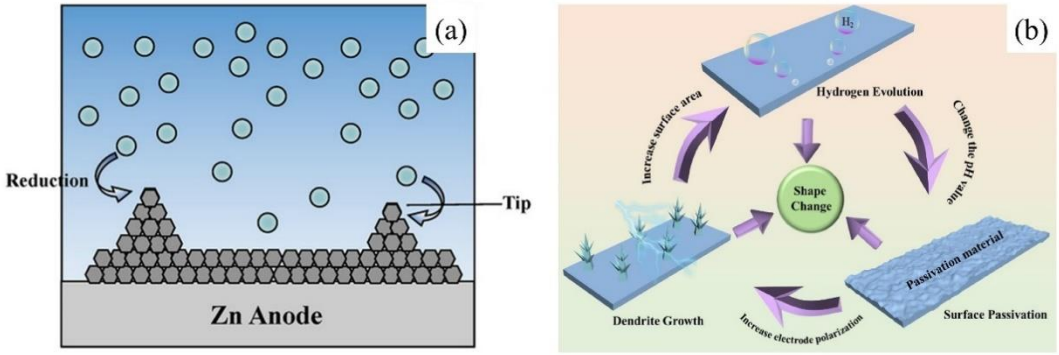

Figure 3 (a) Scheme of tip effect Comprehensive [33](b) Schematic diagram of the relationship of dendritic growth, hydrogen evolution, surface passivation and shape change.[34]

The above three problems will promote each other and eventually lead to electrode failure, as shown in figure 3 (b) [34]. Specifically, the growth of dendrites will increase the surface area of zinc anode and promote HER.[28] During the cycling process, HER leads to the accumulation of hydroxide, which intensifies the occurrence of side reactions/passivation. Eventually, the presence of the passivation layer will increase electrode polarization, leading to more severe dendrite growth. The above three problems promote each other and eventually lead to battery failure. Suppressing the above problems can greatly improve the stability of zinc anode.

1.2 Zn-free anode

Although the above introduction to the advantages, mechanisms, and challenges of zinc anodes suggests that they have significant performance and development potential, zinc metal still serves a dual role as both the active material and the current collector when used as an anode. In reality, only about 10% of the zinc in the anode is actually utilized as active material[35], [36], which significantly reduces the energy density of zinc-ion batteries. Therefore, the concept of an "anode-free" design was proposed, referring to direct platting/stripping on a zinc-free current collector to achieve nearly 100% zinc utilization.[36] Many past and recent studies have demonstrated that various materials can achieve

uniform zinc deposition, making them suitable for use as current collectors in anode-free designs. such as Au[37], Ag[38], Sn[39], [40], Pb[39], Cu[39], [41], Sb[42], Ti_3C_2[43], [44], and MOFs.

Therefore, many optimization strategies for zinc-free anodes have been implemented. For example, Chen's team achieved an attractive energy density of 274 Wh kg^{-1} by constructing Sb/Sb_2Zn_3-heterostructure on the Cu surface. The presence of zinc-philic metals Sb provided abundant nucleation sites for zinc deposition, showing stronger adsorption and uniform electric field distribution during the zinc plating process.[42] In addition to modifying the interface of zinc-free anodes, extensive solvent engineering for zinc-free anodes has also been implemented. Cui's team developed a PC (polycarbonate)-H_2O co-solvent system suitable for Cu anodes. Specifically, the addition of PC effectively helps anions enter the solvation structure to form the SEI (solid-electrolyte interphase). Additionally, PC itself can reduce the activity of water to prevent side reactions. Under this two effect, the Cu metal zinc-free anode exhibits an attractive coulombic efficiency of 99.93% and a cycle life of over 500 cycles.[45]

1.3 MXene

In this section, the composition, structure and synthesis method of Ti_3C_2 materials will be discussed in detail.

1.3.1 Composition and structure of MXene

Since Gogotsi first obtain transition metal nitride/carbide layered material (MXene)[46], MXene has attracted widespread attention due to its high conductivity (20,000 S/cm)[47], excellent mechanical properties (Young's modulus about 0.33 TPa and breaking strength around 17 GPa)[48], diverse structures and adjustable interface functional groups.

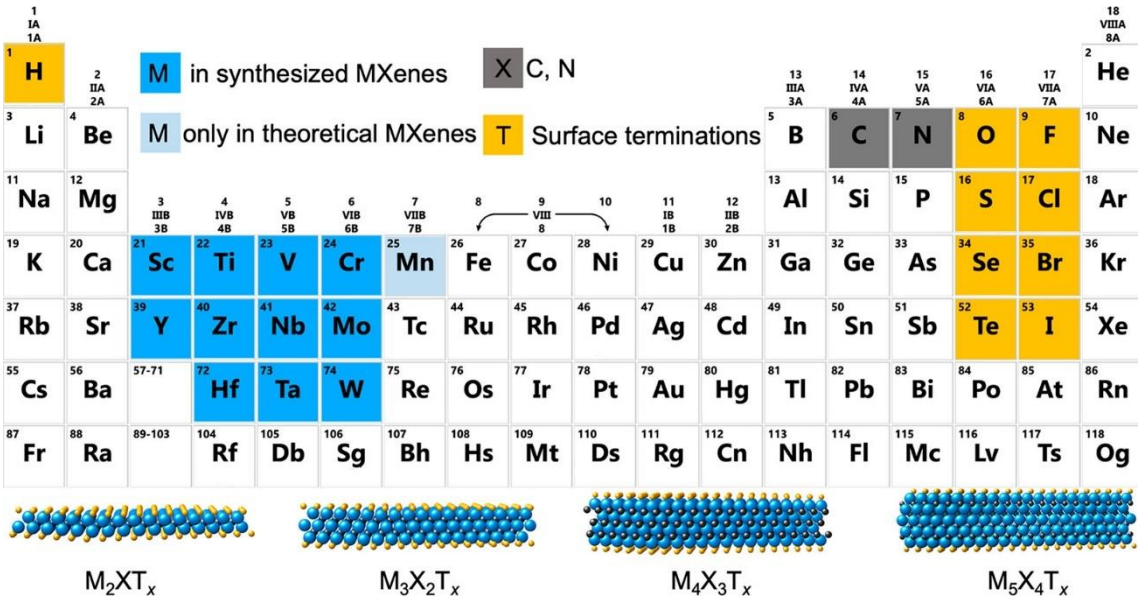

Figure 4 Diversity in MXene composition[49]

MXene ($M_{n+1}X_nT_x$) can be obtained by selective removal of the A layers in MAX ($M_{n+1}AX_n$) phase through a typical etching method, where M stands for early transition metals, A represents A-group elements in the periodic table (mostly IIIA and IVA, like Al and Si), X is either carbon or/and nitrogen, n can vary from 1 to 4, and T_x is terminal groups to stabilize the surface thermodynamics determined by different etchants and etching methods. (figure 4) Single transition metal MXene is the most common structure, like Ti_2CT_X[50], V_2CT_X[51], Ti_2NT_X[52], $Ti_4N_3T_X$[53]. However, because of the instability of nitride MXene in HF solution and the fact that the cohesive energy of $Ti_{n+1}N_n$ is smaller than $Ti_{n+1}C_n$, the preparation of nitride MXene is more complicated than that of carbide MXene which limited the usage of nitride MXene. In addition, double M metal MXenes have also gained significant attention, such as $Mo_2TiC_2T_x$[54], $Mo_{1.33}Y_{0.67}CT_X$[55]. The crystal structures of double-M metal MXenes vary greatly, resulting in the changeable colors and highly tunable electronic properties. [54] $Mo_2TiC_2T_x$ and $Mo_2Ti_2C_3T_x$ are arranged in the order of Mo-Ti-Mo and Mo-Ti-Ti-Mo respectively.[56] While $Ti_yNb_{2-y}CT_x$ and $Nb_yV_{2-y}CT_x$ are random solid solutions whose color changes according to the specific chemical composition. Therefore, various properties of MXene can be changed by adjusting the composition of double M metal MXene. Research have shown that changes in different double M metal MXene compositions can achieve adjustable EMI (electromagnetic interference) shielding effects from 10dB to 60dB with a thickness of ~5 μm at 10 GHz . [54] Divacancy MXene can also be prepared by selectively etching the Al and Sc atoms from designed $(Mo_{2/3}Sc_{1/3})_2AlC$. The divacancy MXene $Mo_{1.33}C$ exhibits a high electrical conductivity and a 65% higher volumetric capacitance than Mo_2C.[55] Recently, inspired by developments in the field of high-entropy compounds, there have been reports on several high-entropy MXenes, providing more possibilities for MXenes. For example, $TiVNbMoC_3T_x$[57], $TiVCrMoC_3T_x$[57], and $(Ti_{1/3}V_{1/6}Zr_{1/6}Nb_{1/6}Ta_{1/6})_2C_xN_{1-x}T_y$[58]. Recent studies have shown that high-entropy MXene leads to excellent photoelectrochemical OER capabilities due to its many metal active sites, high conductivity, and fast reaction kinetics.[59] Moreover, the addition of high-entropy MXene makes the separator have strong lipophilic properties and can uniformly deposit Li^+ on the surface of lithium metal.[60]

1.3.2 Synthesis of MXene

Various synthesis methods also bring different surface functional groups and different morphology to MXene, resulting in diverse properties. The synthesis of MXene can be roughly divided into top-down and bottom-up methods.

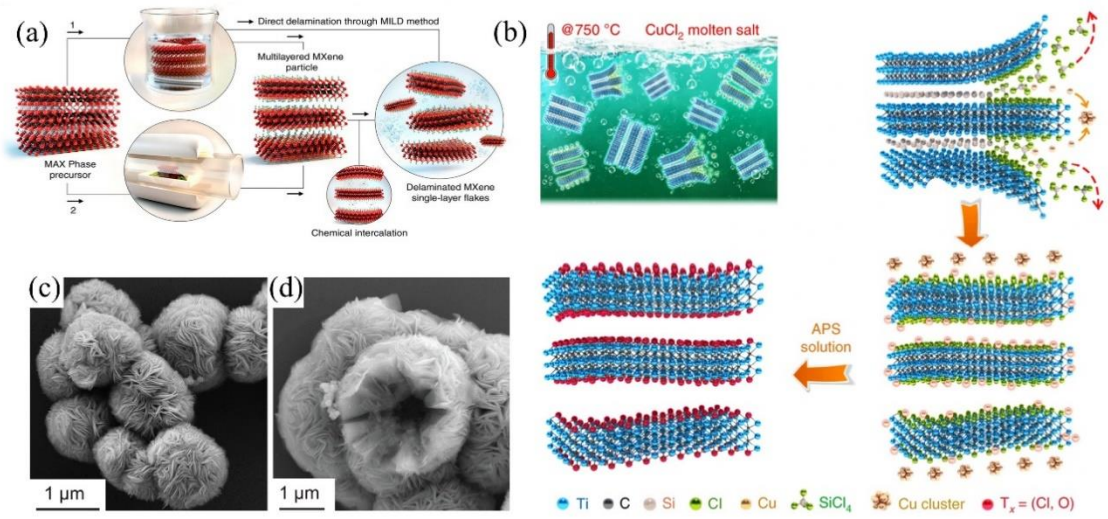

Figure 5 (a) Typical synthesis route of MXene[61] (b) Schematic of $Ti_3C_2T_x$ MXene preparation[62] (c) and (d) Morphologies of CVD-Ti_2CCl_2.[63]

For the top-down method, HF solution etching is the earliest[50] and the most widely used method. After the etching step, an intercalating agent is often used to convert the compact structure into an accordion-like stacked structure, and then mechanically exfoliating (such as ultrasonic treatment) is performed to obtain a single layer or few layers of MXene. (figure 5(a)) The commonly used intercalating agents include dimethyl sulfoxide[64], urea, and isopropyl amine.[52] DFT calculations show that a single layer of Ti_3C_2 has a higher Li capacity and a lower Li diffusion barrier for Li-ion battery.[65] Moreover, during the etching process, negatively charged functional groups such as -O, -OH, -F are often introduced and bring hydrophilicity to the MXene surface. Calculations show that surface functional groups are closely related to the electronic properties of MXene[66]. It has been proven that annealing at 500 degrees in an argon atmosphere is often used to reduce many functional groups on the Ti_2C surface. Subsequently, a high field effect carrier mobility of 10^4 cm^2 V^{-1} s^{-1} was achieved.[67]

However, due to the toxicity and danger of HF, etchants mixed with fluoride salts and hydrochloric acid are also used to replace HF in the synthesis of MXene.[68] Research shows that both HF and LiF/HCl etchants exhibit stepwise etching characteristics. The difference is that LiF/HCl etchant has an intercalating agent that can promote the delamination of MXene. However, LiF/HCl etchant cannot break the grain boundaries of MXene polycrystals due to its mild characteristics, leaving incompletely etched MAX particles and affecting the yield.[69] In terms of functional groups, research shows that LiF/HCl has higher =O and less -F, which may be helpful in increasing the capacity of energy storage devices. [70]

Many efforts have also been invested in developing clean preparation methods due to the environmental issues caused by HF and the introduction of inert -F surface groups, including molten salt etching[53], alkali treatment hydrothermal etching[71], and electrochemical etching[72].$Ti_3C_2Cl_2$ anode can be successfully obtained by soaking Ti_3SiC_2 in $CuCl_2$ Lewis molten salt (figure 5 (b)), showcasing a notable Li^+ storage capacity of 205 mAh g^{-1}.[62] Research also shows that compared to traditional HF etching methods, the APS (ammonium persulfate) added after the etching step during

the molten salt etching may partially oxidize the C in MXene. Moreover, Ti_3C_2 prepared from molten salt does not have –OH surface groups, thus reducing the hydrophilicity of the surface.[62] At the same time, a variety of synthetic methods have also been applied to achieve specific functional groups on the MXene surface. Ammonia and Ti_3C_2 can be used to synthesize Ti_3C_2-NH_2 nanosheets through a straightforward sealed thermal method. The presence of -NH_2 effectively enhances the mechanical strength of MXene materials.[73], [74] MXenes with amide- and imino-terminated surfaces can be synthesized by reacting halogen-terminated MXenes with deprotonated organic amines[75]. Furthermore, the presence of surface functional groups can also help with the doping of surface atoms. Benefiting from the stronger hybridization between surface O 2p and Co 3d orbitals, Co@V_2CTx successfully synthesised using iced photochemical reduction method. As a result, an OER overpotential of 242 mV and a HER overpotential of 35 mV at 10 mA cm^{-2} were achieved. [76]

Recently, due to the pursuit of large-scale and controllable production of MXene, many bottle-top methods have been studied, such as chemical vapor deposition (CVD)[77], ion sputtering[78] and wet chemical amalgamation[79]. These methods tend to have higher controllability, uniformity, and scalability. Using CH_4 as the carbon source and copper foil placed on the molybdenum foil as the catalyst for CVD, large-area and uniform 2D ultra-thin α-Mo_2C crystals can be produced. Moreover, the size, thickness, and morphology of Mo_2C crystals can be controlled by adjusting the growth time and temperature.[77] With the controllable composition and morphology, MXene also produces many interesting properties. Under zero magnetic field, the resistance of CVD-Mo_2C begins to decrease at 3.6 K and drops to zero at 2.76 K, indicating the onset of superconductivity. [77]It is worth noting that bottle-up methods also bring more possibilities to the morphology of MXene. Research has shown that Ti_2CCl_2 grown on the Ti surface by CVD at 950°C using a gas mixture of CH_4 and $TiCl_4$ diluted in argon shows a distinctive "flower-like" vesicle morphology (figure 5 (c)(d)), formed by buckling and releasing the MXene carpet to expose new surfaces for further reactions. These flower-like MXenes exhibit relatively higher capacitance. If the mechanism is further studied and the morphology is adjusted, potential application value is expected to be realized. [63]

In short, MXene's high conductivity, good mechanical strength, diverse composition and surface functional groups make it show rich possibilities in electrochemical energy storage. Research and development of MXene has far-reaching significance for electrochemical energy storage.

1.3.3 Ti_3C_2 Zn-free anode

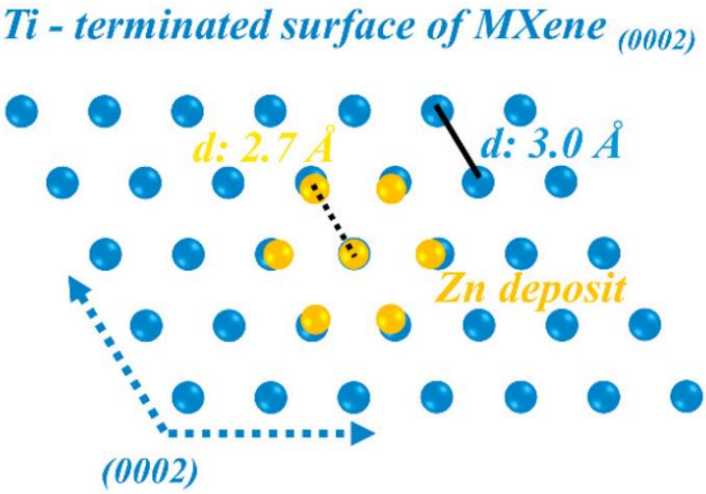

Figure 6 Atomic arrangements of Ti terminated surface of Ti_3C_2Tx MXene (0002) and Zn deposits (0002) and their small lattice mismatch.[44]

As mentioned above, the high conductivity, good mechanical strength, diverse composition and surface functional groups of MXene make MXene-based zinc-free anodes possible. Among all MXene, Ti_3C_2 has attracted significant attention due to its (1) low lattice mismatch (within ~10%) with Zn metal (figure 6)[35] [44] (2) good ionic conductivity (20,000 S cm^{-1}) and mechanical properties[47] (3) Sufficient hydrophilicity, which is rare in 2D materials and promotes better interaction with the electrolyte.

For example, Chen et al. used a facile solution casting method to prepare $Ti_3C_2T_x$/nanocellulose composite films and used them for zinc-free anodes. The study showed that the low crystal mismatch of (002) between Ti_3C_2 and Zinc facilitated the directional deposition of Zn along (002). Under the synergistic effect, the film exhibited excellent mechanical properties, electrical conductivity, wettability, and higher Coulombic efficiency for Zinc platting and stripping.[43]

1.4 Co-solvent Engineering

Although the Zn anode has superior capacity and attractive safety, its cycling stability is still affected by HER, dendrite growth, and side reactions mentioned in chapter 1.1.2. Co-solvent engineering is one of the most direct and feasible solutions for improving the stability of zinc anodes and zinc-free anodes. Common co-solvent engineering strategies mainly functionalize from the following aspects : (1) breaking the hydrogen bond network. (2) adjusting the solvation structure. (3) adsorption.

1.4.1 Breaking the hydrogen bond network

One of the direct impacts of adding co-solvents to aqueous electrolytes is changing the structure of water. Hydrogen bond networks spontaneously form in pure water due to water's proton donor and acceptor amphipathic abilities. When water molecules form hydrogen bonds with each other, the OH covalent bonds within the water molecules are weakened, resulting in increased HER activity. [80]Therefore, many solvents with strong nucleophilic functional groups are added to water to form the

hydrogen bond with water and break the original hydrogen bond network, thus improving the stability of water.

For instance, Diglyme (DGM) with ether and alcohol functional groups can effectively break the hydrogen bond network of water, thereby suppressing the water decomposition reaction on the Zn anode surface. As the content of DGM increases, the blue shift of the Raman peak reflects the weakening of hydrogen bonding interactions.[81] At the same time, the peaks narrow to high frequency, which reflects a reduced proportion of strong hydrogen bonds in the solution. At -20°C, Zn||Zn symmetrical battery cycled for 5200h at 1mA cm^{-2} and 1mAh cm^{-2}. Highly polar Tetramethylurea (TMU) can also break the hydrogen bond network. Zn||Cu batteries using TMU-based electrolytes can operate stably for more than 6000 times at a current density of 10 mA cm^{-2}, with a Coulombic efficiency of 99.8%.[82]

1.4.2 Adjusting the solvation structure

Apart from the effect between the co-solvent and water, the effect between the co-solvent and zinc ions is also important. In pure H_2O solvent, dissolved zinc ions will solvate with polar solvents in electrolytes. For example, in an aqueous solution of $ZnSO_4$ salt, Zn ions will form an octahedral $[Zn(H_2O)_6]^{2+}$ structure with 6 H_2O molecules.[83] during the desolvation process of zinc ion deposition, the H_2O molecules released by the hydrated zinc ions on the electrode surface will be reduced. Studies have pointed out that the H_2O molecules produced by desolvation have weaker O-H covalent bonds and are therefore less stable.[84] Furthermore, water solvated with zinc ions is the main cause of the HER reaction, rather than free water without bonding with Zn ion.[85] Therefore, reducing the content of H_2O molecules in the solvation sheath is important for the stability of zinc anodes.

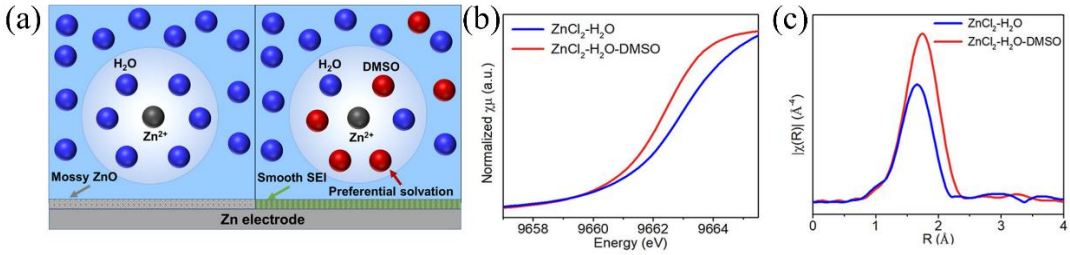

Figure 7 (a) Scheme of Zn^{2+} solvation structure and zinc surface passivation in H_2O (left) and H_2O–DMSO (right) solvents. (b) X-ray absorption near-edge structure (XANES) and (c) Fourier transformed extended X-ray absorption fine structure (ft-EXAFS) spectra of $ZnCl_2$–H_2O–DMSO and $ZnCl_2$–H_2O electrolytes.[86]

A common strategy is to introduce co-solvent into the solvation sheath to reduce the water content in the solvation sheath. Solvents with a high donor number (DN) and dielectric constant (ε) like DMSO[86], dimethyl carbonate (DMC), 1,2-dimethoxyethane (DME)[87], N,N-dimethylformamide (DMF)[88], N, N-dimethyl acetamide (DMA)[89], [90] are added to the aqueous electrolyte to compete with water to enter the solvation structure. The donor number is a measure of Lewis basicity. In electrolytes, solvents with higher donor numbers are more nucleophilic, have stronger solubility, and are more likely to coordinate with Zn^{2+}. The dielectric constant reflects the polarity of solvent molecules. Solvents with higher dielectric constants tend to have higher polarity and stronger solubility. [86], [91] DMSO with a high donor number (29.8) and dielectric constant is added to the ZnCl-H_2O electrolyte, which can preferentially solvate with Zn^{2+} and have a strong interaction with H_2O to reduce water decomposition

(figure 7 (a)). X-ray absorption near-edge structure (XANES) spectra show that the addition of DMSO leads to a shift of the edge position to lower energy, which means the reduction of bonding strength between Zn ions and H_2O (figure 7 (b)). Furthermore, Fourier transformed extended X-ray absorption fine structure (ft-EXAFS) also indicated that the Zn–O bond length increases. This may indicate that the coordination between Zn ions and the solvent is weakened with the DMSO involved (figure 7 (c)). Therefore, the addition of DMSO co-solvent replaces the water in the solvation sheath and inhibits the hydrogen evolution reaction. In addition, DMSO entering the solvation sheath can also help form SEI, further enhancing the cyclic stability of Zn deposition. Consequently, the anode of the Ti||Zn half-cell has a high average coulombic efficiency of 99.5% within 400 hours.[86]

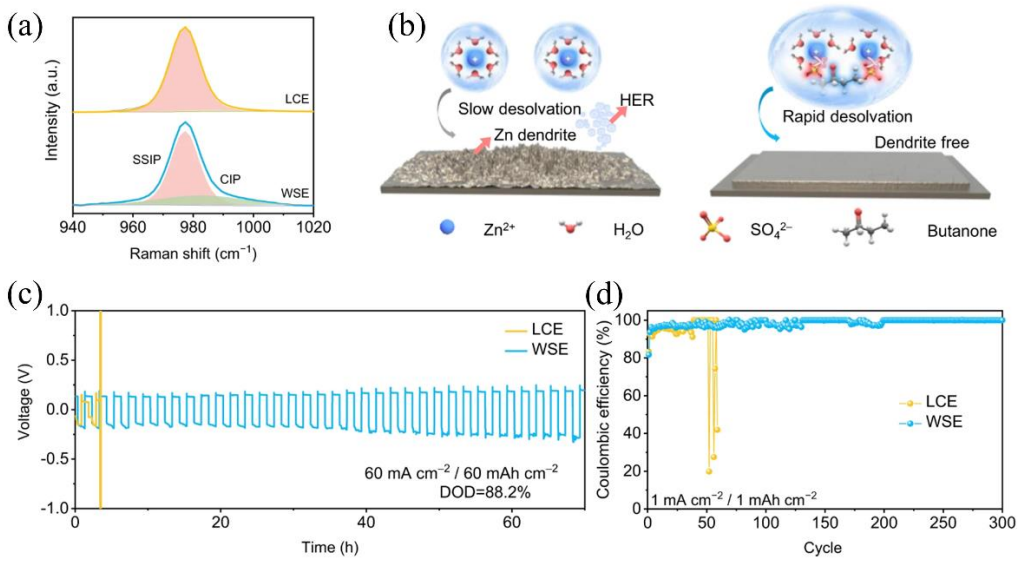

Figure 8 (a) Raman spectra of weakly solvating electrolyte (WSE, water, co-solvent (additive), and electrolyte salt) and low-concentration electrolyte (LCE, 0.5 M $ZnSO_4/H_2O$) (b) Schematic diagram of how Zn anode works in WSE and LSE (c) Galvanostatic cycling profiles of symmetric cells with LCE and WSE at 60 mA/60 mAh cm^{-2}. (d) Coulombic efficiency (CE) measurements of Ti||Zn cells under different electrolyte systems at 1 mA/1 mAh cm^{-2} [91]

Although this strategy of adding a solvent with strong solvating ability can reduce the water content in the solvation sheath, it also hinders the desolvation kinetics to a certain extent. Similarly, many weak solvation strategies have also been studied, that is, using low donor numbers and low dielectric constant solvents to limit the solvation of water molecules.[91], [92], [93]Introducing butanone (DN=18.5; ε=17.4) into the $ZnSO_4$ aqueous electrolyte can effectively reduce the amount of solvated water and enhance the Zn ion desolvation kinetics. Butanone with a low dielectric constant will effectively reduce the solvation of the solvent and Zn ions, thereby promoting the bonding of Zn ions and SO_4^{2-} ions. This is demonstrated in the Raman spectrum (figure 8 (a)). The coexistence of solvent-separated ion pair (SSIP) and contact ion pair (CIP) was observed in the electrolyte added with butanone, illustrating that the anion enters the solvated structure (figure 8 (b)). In summary, the addition of butanone introduced OTF^- into the solvation sheath of zinc ions, effectively inhibiting hydrogen evolution. At the same time, the negatively charged OTF^- is also easier to desolvate, resulting in faster zinc deposition kinetics. Ti||Zn cell can provide a cycle life of 600 h and a Coulombic efficiency of 99.9% under 0.5 mAh cm^{-2} and 1mA cm^{-2} and maintain a 70 h stability under conditions of high current density (60 mA cm^{-2}) and high capacity (60 mAh cm^{-2})(figure 8 (c)(d)). [91]

1.4.3 Adsorption

The adsorption of co-solvents at the Zn metal interface is also often reported, but different adsorption behaviors play different roles in the process of Zn metal deposition. For example, DEC co-solvent can form a hydrophobic structure on the surface of zinc anode, effectively inhibiting HER. The addition of DEC co-solvent can effectively adsorb on the Zn surface to form a water-poor electric double layer. As shown in the figure 9 (a)(b), molecular dynamics (MD) calculations were applied to demonstrate the interfacial chemistry under the DEC cosolvent system. Within 3 nm of the zinc surface, the density of water molecules decreases from 18.79 nm^{-2} (H_2O) to 7.04 nm^{-2}(H_2O-DEC). DFT calculations also show that compared with water molecules, DEC has a more negative adsorption energy, leading to a more easily adsorbed on the zinc surface (figure 9 (c))[94]. Due to the ether oxygen in PEG, PEG can be adsorbed parallel to the Zn surface. This adsorption can effectively hinder the two-dimensional diffusion of the Zn surface and reduce the exchange current density of Zn deposition [95], thereby inhibiting the growth of dendrites. In addition, the characteristic adsorption of PEG on the specific crystal orientation of the zinc metal surface can also help Zn to deposit along the (002) direction. This specific growth direction parallel to the plane is conducive to alleviating the formation of dendrites.[96]

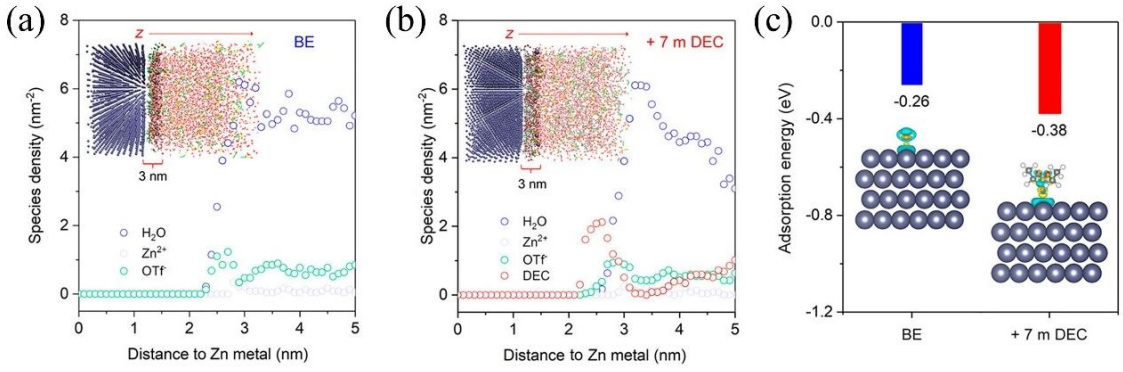

Figure 9 Snapshots and species density profiles of MD simulations in the direction perpendicular to Zn surface for (a) BE and (b) BE + 7 m DEC. (c) The adsorption energy and charge density difference of H_2O and a DEC molecule on the Zn(002) surface. Yellow and cyan clouds indicate electron accumulation and depletion, respectively. The isovalue is 0.001 e $Bohr^{-3}$. [94]

1.5 Scope of Research

Compared with zinc anodes, the Ti_3C_2 zinc-free anode offers higher zinc utilization, which can effectively improve the energy density of zinc-ion batteries (ZIBs). However, the challenges of hydrogen evolution reaction (HER), dendrite growth, and side reactions that are prevalent in zinc anodes will also appear in Ti_3C_2 zinc-free anodes, resulting in a low Zn plating/stripping coulombic efficiency and a moderate cycling life. Therefore, reasonable modification of the electrolytes is necessary to solve the afore-mentioned issues and further improves the reversibility of Zn deposition on Ti_3C_2 zinc-free anode.

Here, PEG (polyethylene glycol) and IPA (isopropanol) is chosen as the co-solvent to engineering the widely used $Zn(OTF)_2$ (Zinc trifluoromethanesulfonate) aqueous electrolytes and the Zn deposition behavior on $Ti_3C_2T_x$ MXene in different electrolytes are investigated. We find that the introduction of the co-solvents can enhance the coulombic efficiency of Zn plating/stripping on MXene. The role of PEG

co-solvent in the zinc deposition process is reflected in (1) inhibiting hydrogen evolution and (2) affecting the growth and texture of zinc. Similarly, IPA co-solvent can also (1) inhibit hydrogen evolution and (2) affect the growth and texture of zinc during zinc deposition. (3) Forming SEI layer. All these improvements will benefit the uniform deposition of Zn, thereby enhancing the coulombic efficiency and cycle life of the Ti_3C_2 zinc-free anode.

The research questions for the master's thesis that naturally arise at this point are:

1. *Can co-solvent engineering improve the stability of Ti_3C_2 zinc-free anode?*
2. *What role do the PEG and IPA co-solvent play in enhancing the stability of Ti_3C_2 zinc-free anode?*

Before presenting the experimental results, the details of the experiment need to be discussed first.

2 Experimental

In this section, experimental details like material synthesis, battery assembly, and the background of various characterizations will be introduced.

2.1 Material synthesis

2.1.1 Synthesis of Ti_3C_2

1 g of Ti_3AlC_2 MAX phase powder (11 Technology Co. Ltd) and 1.6 g of LiF powder (Alfa Aesar, 98.5%) were mixed in 20 mL of 9 M HCl. Then, etching was carried out for 24 hours at 35°C with a stirring speed of 500 RPM (Eppendorf Centrifuge 5804). After etching, the sediment was washed with deionized water until the pH of the supernatant reached 6. The slurry was then collected and ultrasonicated for 1 hour and centrifuge for 30 minutes at 3500 RPM to delaminate, followed by vacuum filtration through a membrane (Jinteng, 0.2 µm pore size) to get a self-standing film. This film will be used as the working electrode.

2.1.2 Preparation of electrolyte

1M $Zn(OTF)_2$ was dissolved in a solution with a volume ratio of IPA:H_2O = 1:1, which was labeled as 50%IPA (IPA). In order to keep the water content unchanged, 1M $Zn(OTF)_2$ was dissolved in a solution with a volume ratio of PEG:H_2O = 1:1, which was labeled as 50%PEG (PEG).

2.1.3 Cell Assembly

Assembly of Zn||Zn symmetric cell: The anode and cathode of CR2032 coin cell are both zinc metal foil (100µm), and the separator is GF/A (Waterman). The assembly order of the battery is zinc foil-separator-zinc foil-stainless steel plate (1mm)-spacer.

Assembly of Ti_3C_2||Zn half-cell: The anode is 100 um Zinc foil with a diameter of 14 mm, cathode is Ti_3C_2 film with a diameter of 14 mm, and the separator is GF/A (Waterman). The assembly order of the battery is Ti_3C_2 -separator-zinc foil-stainless steel plate (1mm)-spacer.

Beaker cell: The cathode is 0.5 cm^2 Ti_3C_2 and the anode is 0.5 cm^2 zinc foil. The two electrodes will be placed in 20ml of prepared electrolyte.

2.2 Material characterization

2.2.1 Fourier-transform infrared spectroscopy (FTIR)

Fourier-transform infrared spectroscopy is a technique that obtains the molecular vibration of a sample by analyzing its absorption spectrum. [97] It is often used to analyze changes in chemical bonds. In the mid-infrared region (4000–1000 cm^{-1}), two main types of vibrations are observed: vibrations along the chemical bonds, called stretching vibrations (v), which involve changes in bond lengths; and vibrations

involving changes in bond angles, specifically bending vibrations (δ - in-plane, π - out-of-plane). The position of the absorption peak is related to the bond strength and the mass of the vibrating atom. The stronger the bond, the higher the absorption frequency.

2.2.2 X-ray diffraction (XRD)

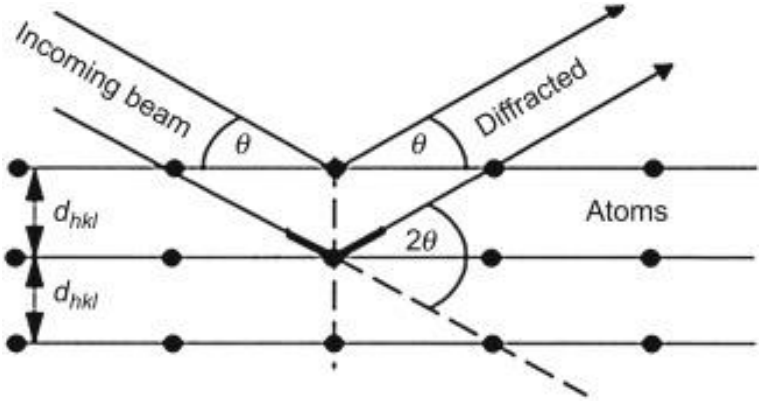

Figure 10 Geometrical condition for diffraction from lattice planes[98]

X-ray diffraction is a common method for characterizing crystalline materials. When X-rays reach a sample, multiple scatterings occur. Among them, elastic scattering of photons and electrons around atomic nuclei can keep the energy unchanged and maintain a phase relationship with the incident wave. However, due to the periodicity of the crystal structure, constructive or destructive scattering will occur, thus showing the characteristic diffraction of the crystal.

The above process can be determined by Bragg's law: $n\lambda = 2d_{hkl}sin\theta$. As shown in figure 10, n is the diffraction order, λ is the wavelength of the incident beam (in nanometers), d_{hkl} is the lattice spacing (in nanometers), and θ is the angle of the diffracted beam (in degrees). [98]

In this work, XRD was mainly used to characterize the orientation of Zn deposition on the Ti_3C_2 surface, especially the ratio of (002)/(101) for Zn growth orientation. Measurements were taken on an X'Pert Pro diffractometer (PANalytical, 45 kV & 40 mA) with Cu-Kα (λ= 1.54 A) radiation.

2.2.3 Scanning Electron Microscopy (SEM)

A scanning electron microscope (SEM) is an electron microscope that obtains sample morphology information by scanning the sample surface with an electron beam. When electrons are emitted to the sample surface, they interact with the atoms on the sample surface to produce various signals containing the sample surface (such as secondary electrons, etc.). These signals are combined with the position of the light beam to produce an observable image. [99]

In this study, SEM was used to observe the morphology of Zn deposition on the Ti_3C_2 surface after cycling in different solvents.

2.2.4 X-ray photoelectron spectroscopy (XPS)

XPS is a surface-sensitive quantitative spectroscopy technique. It can be used to measure the elemental composition inside a sample, as well as the chemical state of the surface elements. When used in combination with ion beam etching, it can be used to analyze the composition and chemical state of samples at different depths. The principle of XPS is based on the photoelectric effect (figure 11), which produces electron emission when high-energy photons hit a material. The kinetic energy of the photoelectron is given by Einstein's law:[100], [101]

$$KE = h\nu - BE \tag{18}$$

where $h\nu$ is the energy of the incident radiation and BE is the binding energy of the electron at a particular energy level.

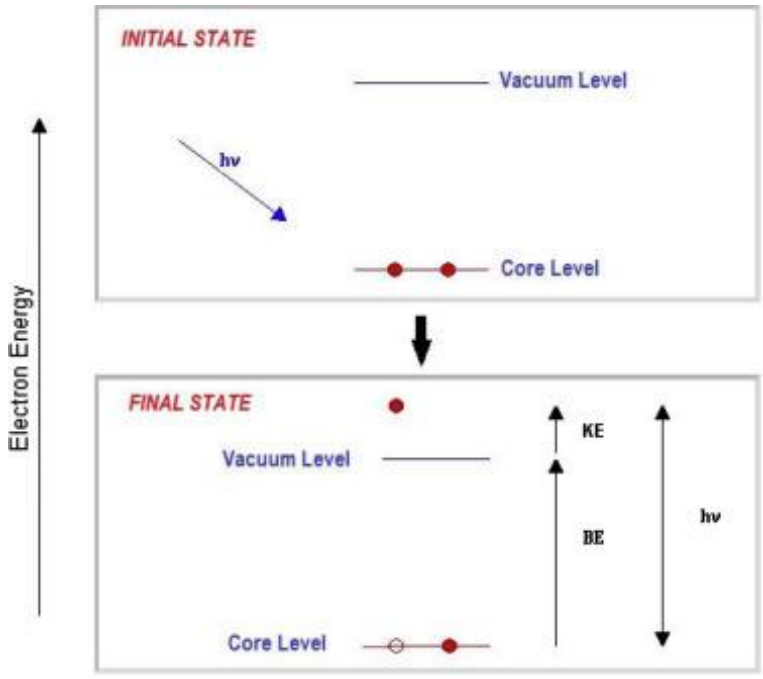

Figure 11 The photoemission process in X-ray photoelectron spectroscopy analysis. The *solid circles* represent electrons and the *horizontal lines* represent energy levels within the material being analyzed.[101]

The BE of the electrons can be obtained by measuring the kinetic energy of the emitted electrons, thereby determining the elemental composition and chemical state within the sample surface area.

In this work, XPS was used to characterize the composition of the SEI on the Ti_3C_2 surface after cycling in different electrolyte systems using a ThermoFisher K-Alpha surface spectrometer with a monochromatic Al Kα (1486.6 eV). The binding energy was corrected for the charge shift using the primary C1s hydrocarbon peak at BE = 284.8 eV as a reference. The data were deconvolved using the Lorentzian/Gaussian mixture fitting method in the ThermoFisher Avantage software.

2.3 Electrochemical characterization

2.3.1 Galvanostatic Charge and Discharge (GCD)

Galvanostatic Charge and Discharge (GCD) is a commonly used charge and discharge characterization method, which is often used to characterize the capacity, efficiency, cycle life, and rate performance of electrochemical devices. Specifically, GCD will maintain a constant current through the electrochemical device to record voltage feedback to reflect the various performance of the electrochemical device.

In this work, the coulombic efficiency and cycle life of the Ti_3C_2||Zn half-cell are characterized by GCD. The assembled coin cell is first discharged at a constant current of 1mA cm^{-2} for 1mAh cm^{-2}(Q_d), then charged at a constant current of 1mA cm^{-2} to 0.5 V (all active Zn is stripped) and the charge capacity is recorded as Q_c. During this cycle, and the coulombic efficiency of this cycle is:

$$CE = \frac{Q_c}{Q_d} \times 100\% \tag{19}$$

After one cycle is completed, the same cycle is continued until the cell short circuits or fails, and the cycle life of the half-cell can be obtained.

Therefore, the average Coulomb efficiency is:

$$ACE = \frac{\sum CE_i}{i_{max}} \tag{20}$$

Where i is cycle number, CE_i is the Coulombic efficiency of the i cycle, i_{max} is cycle life of the cell.

The cycle life of the Zn||Zn symmetric cell is also characterized by GCD. The assembled symmetric cell is first discharged at a constant current of 1mA cm^{-2} for 1mAh cm^{-2}, and then charged at a constant current of 1mA cm^{-2} for 1mAh cm^{-2}. This is considered as a cycle. The time it takes to charge and discharge repeatedly in this way until the battery is damaged is recorded as the cycle life.

2.3.2 Electrochemical Impedance Spectroscopy (EIS)

Electrochemical impedance spectroscopy (EIS) provides kinetic and mechanistic data for a variety of electrochemical systems. EIS is based on the perturbation of an electrochemical system by applying a sinusoidal signal (AC voltage or AC current) over a wide frequency range and monitoring the sinusoidal response of the system to the applied perturbation (current or voltage, respectively).[102]

Here the focus is on elucidating the components of the Nyquist plot. By applying a small AC voltage and measuring the resulting AC current, we can establish the impedance relationship between the input (AC voltage) and the output (AC current). This relationship, expressed as a "transfer function," is depicted on the Nyquist plot with the real part of the impedance on the horizontal axis and the imaginary part of the impedance on the vertical axis. The plot provides valuable insights into the electrochemical system.

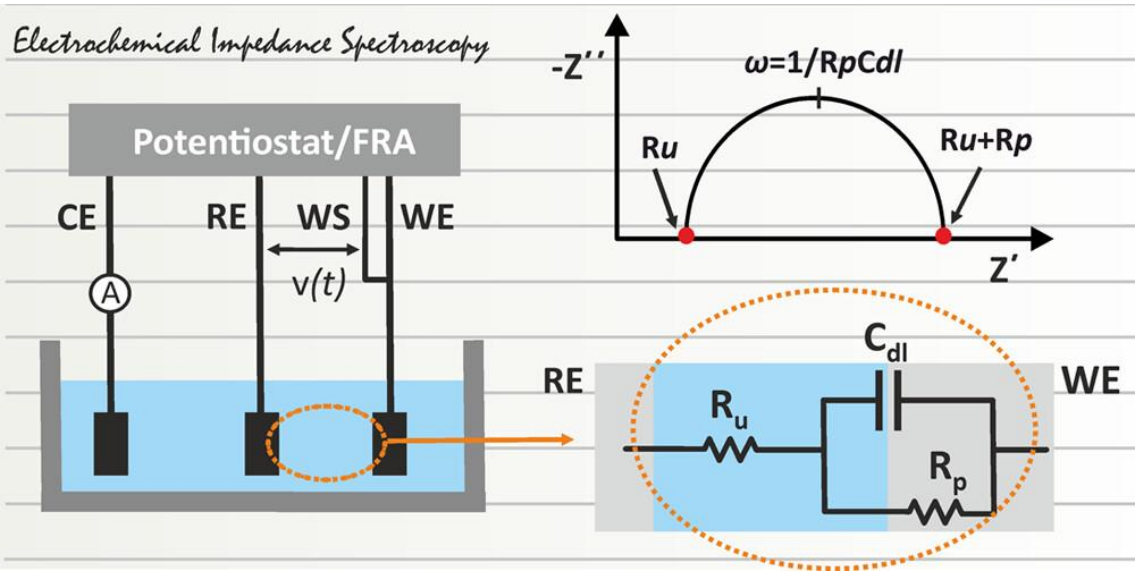

Figure 12 Typical three-electrode and its equivalent circuit and Nyquist plot[102]

To interpret the Nyquist plot, various equivalent circuits were developed to analyze the associated electrochemical processes[103]. Figure 12 illustrates a classic equivalent circuit model. In this model, R_u represents the uncompensated resistance, defined as the ohmic impedance of the electrolyte between the working and reference electrodes. Theoretically, R_u also includes the impedance of the material and the metal connections. C_{dl} denotes the double layer capacitance, which corresponds to the charging and discharging of the double layer. This response is typically faster than that of charge transfer. R_p signifies the polarization resistance, which encompasses both charge transfer polarization and concentration polarization. When the electrochemical process is governed by charge transfer polarization, R_p can be considered a resistor (R_{ct}. According to the equivalent circuit, the impedance can be obtained as:

$$Z = R_u + \frac{1}{j\omega C_{dl} + \frac{1}{R_{ct}}} \tag{21}$$

From the above formula, the real and imaginary parts of Z can be expressed as:

$$Z_{Re} = R_u + \frac{R_{ct}}{1 + \omega^2 {C_{dl}}^2 {R_{ct}}^2} \tag{22}$$

$$Z_{Im} = \frac{\omega C_{dl} {R_{ct}}^2}{1 + \omega^2 {C_{dl}}^2 {R_{ct}}^2} \tag{23}$$

Obviously, from (22) (23), the relationship between the real part and the imaginary part is:[102], [103]

$$\left(Z_{Re} - R_u - \frac{R_{ct}}{2}\right)^2 + {Z_{Im}}^2 = \left(\frac{R_{ct}}{2}\right)^2 \tag{24}$$

Combined with equation (24), the corresponding meaning in Figure 13 can be explained. The first intersection of the Nyquist Plot and the X-axis is R_u, and the second focus is the sum of the electrochemical impedance and the solution impedance.

In this work, EIS is used to measure the ionic conductivity of the electrolyte. The anode and cathode in the tested coin cell are both stainless steel plates (1mm), and the separator is GF/A. The ionic conductivity of the electrolyte can be obtained by the formula:

$$\sigma = \frac{d}{R_u \cdot S} \tag{25}$$

Where σ is ionic conductivity, d is the distance between the electrodes, R_u is ohmic resistance of electrolyte, S is surface area of working electrode.

2.3.3 linear sweep voltammetry (LSV)

Linear sweep voltammetry (LSV) is a voltammetry method in which a current response is obtained by controlling a linear change in voltage. This method can detect the electrochemical current response within the corresponding voltage range.

In this study, LSV was used to detect the electrochemical reaction window and the extent of hydrogen evolution reaction. Specifically, in the three-electrode system, Ti foil was used for both the working electrode and the counter electrode, and Ag wire was used as the reference electrode to detect the specific hydrogen evolution potential.

2.3.4 Cyclic Voltammetry (CV)

Similar to LSV, the potential is still controlled to change linearly, and the current response is recorded during the test. The difference is that when the potential reaches the set potential, the working electrode will scan in the reverse direction until the potential returns to the initial potential. [104]

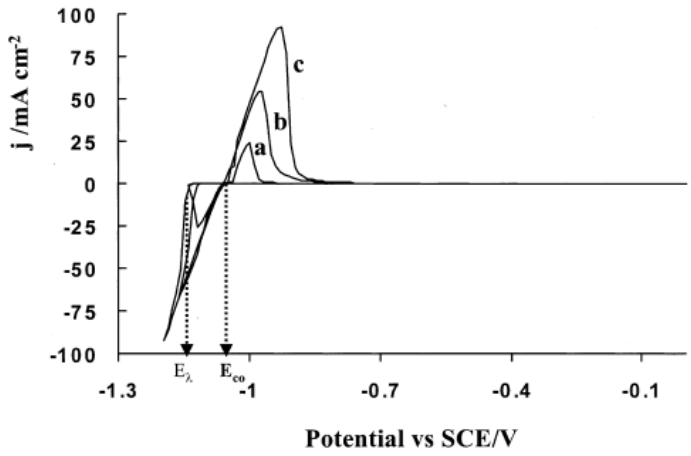

Figure 13 Typical CV curve of Zn deposition on glassy carbon[105]

Figure 13 shows a typical CV curve of zinc deposition. Wherein, E_λ and E_{co} represent switching potential and crossover potential respectively. Switching potential means the potential that overcomes the overpotential and causes rapid current growth during cathode scanning. When the scan is reversed into the anode scan, a focus is generated with the cathode scan curve, which is called the crossover potential, and is also approximately considered to be the equilibrium potential of zinc ions/zinc. Therefore, the overpotential can be expressed as the difference between E_λ and E_{co}.[105]

In this work, CV was used to characterize the overpotential for Zn deposition on Ti_3C_2 surfaces. A two-electrode system was used, where the working electrode was Ti_3C_2, and the counter electrode was Zn.

2.3.5 Chronoamperometry (CA)

Chronoamperometry is an electrochemical test method that applies a stepped constant potential to the working electrode and records the current time response. The typical zinc chronoamperometric response has been discussed in detail in 1.1.1 and will not be repeated here.

In this work, chronoamperometry was used to characterize the zinc deposition process and to investigate the role of the electrolyte in the zinc deposition process. A Zn||Zn symmetric cell was assembled for testing.

3 PEG co-solvent for improved stability of the Ti_3C_2 Zinc-free anode

We mentioned the adsorption behavior of PEG on the zinc surface to inhibit 2D diffusion. In addition, PEG has also been developed to have a variety of effects, such as inhibiting hydrogen evolution[106], regulating deposition orientation[96], etc. Here, we add PEG as a co-solvent to the aqueous electrolyte. FTIR was first employed to investigate the changes in the chemical structure of the electrolyte solution after the addition of PEG. LSV was then used to study the effect of PEG addition on the hydrogen evolution reaction. Subsequently, the deposition behavior of zinc on the Ti_3C_2 surface was analyzed by GCD, CV, CA, SEM and XRD. Finally, coulombic efficiency and cycle life are tested by GCD to confirm the effect of the above changes on the stability of Ti_3C_2 zinc-free anode.

3.1 Inhibition of hydrogen evolution

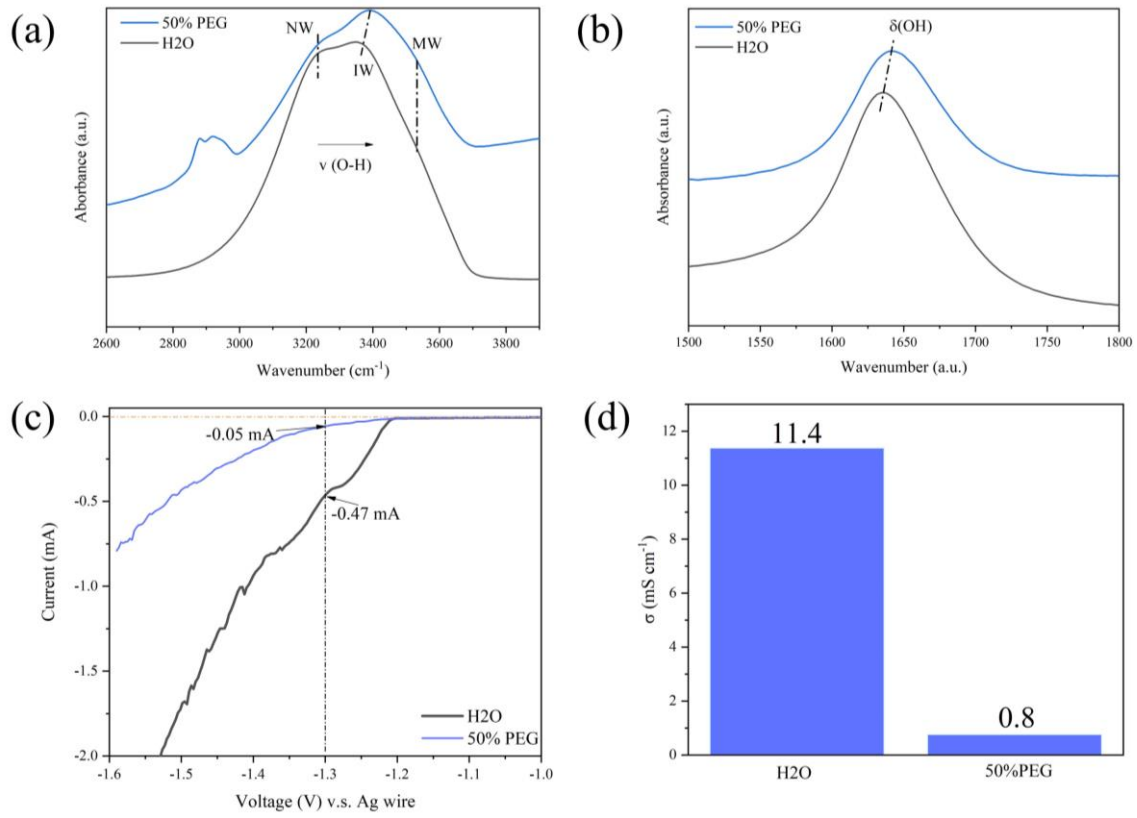

Figure 14 FTIR spectrum (a) 2600cm^{-1}-3900cm^{-1} (b) 1500cm^{-1}-1800cm^{-1} (c) LSV results (d) Conductivity of different electrolyte systems

The electrolyte system in which 1M $Zn(OTF)_2$ is dissolved in H_2O is denoted as H_2O. The electrolyte system in which 1M $Zn(OTF)_2$ is dissolved in a solvent with a volume ratio of PEG:H_2O=1:1 is denoted as 50%PEG. All electrolytes contain 1M $Zn(OTF)_2$. As described in Chapter 1.4.1, since hydrogen bonds and OH covalent bonds share an oxygen atom, breaking a hydrogen bond results in the strengthening of the OH covalent bond. The strengthened OH covalent bonds enhance the stability of

water, leading to the inhibition of the HER. Consequently, disrupting the hydrogen-bonding network is often crucial in suppressing hydrogen evolution. [45]

Figure 14 (a) (b) shows the FTIR spectra of the 50% PEG and H_2O electrolyte groups. The O-H stretching vibrations were recorded in the range of 2600 to 3900 cm^{-1} (figure 14 (a)). This broad peak shown in figure 14 (a) can be classified into "network water (NW)," "intermediate water (IW)," and "multimer water (MW)" according to Gaussian fitting. More specifically, NW molecules arise from a network of hydrogen bonds that are constantly being formed and broken, roughly connected in a tetrahedral structure, almost like in ice. IW molecules can connect with other water molecules but cannot form fully connected patches. IW molecules are roughly generated at the interface of long-distance networks or in short-lived water aggregates. MW does not have the same supramolecular connectivity as NW and IW and mostly exists as free monomers, dimers, and trimers. [81], [107], [108] The figure shows a decrease in the intensity of NW, indicating that the addition of PEG effectively disrupts the hydrogen bond network. This disruption may be attributed to the large number of nucleophilic oxygen atoms in the polymer PEG can compete with H_2O molecules for coordination, attracting part of the water in the hydrogen bond network. At the same time, the IW peak and O-H bending vibration (figure 14 (b)) undergoes a blue shift. This blue shift can also be attributed to the oxygen in PEG forming coordination bonds, thereby altering the coordination environment of water. [45] [109] Therefore, it can be confirmed that the addition of PEG changes the original hydrogen bond network in water, which may be conducive to alleviating the hydrogen evolution reaction.

The LSV was subsequently performed in the 50% PEG and H_2O system to examine the effect of PEG addition on the hydrogen evolution reaction. The scan range was from open circuit potential to -1.6 V vs. Ag wire at a scan rate of 5 mV/s. Comparing the 50% PEG and H_2O groups, the currents were 0.05 mA and 0.47 mA at a potential of 1.3 V vs Ag wire, respectively. The lower current means that less H_2 is released at the same potential. This is consistent with the FTIR results.

It is worth noting that although the 50% PEG bulk electrolyte exhibits good electrochemical stability, it still has a lower conductivity. As shown in Figure 14 (d), the conductivity of the H_2O group is 11.4 mS cm^{-1}, while the conductivity of the 50% PEG group is only 0.8 mS cm^{-1}. The lower conductivity may lead to a larger concentration polarization and thus a larger overpotential, which will be discussed in the next section.

3.2 Deposition behavior

In this section, we investigate the Zn plating/stripping process on Ti_3C_2 in H_2O and 50% PEG electrolytes. Specifically, the deposition of zinc on the Ti_3C_2 surface can be roughly divided into two stages. The first stage is the deposition of Zn on the pristine Ti_3C_2 surface. The second stage is the further deposition of Zn on the primarily deposited Zn surface. The electrochemical methods such as GCD, CV and CA are used to characterize the behavior of zinc in these two steps. SEM and XRD will be performed to verify the morphology and orientation of the zinc deposition.

3.2.1 Deposition of zinc on Ti_3C_2 surface

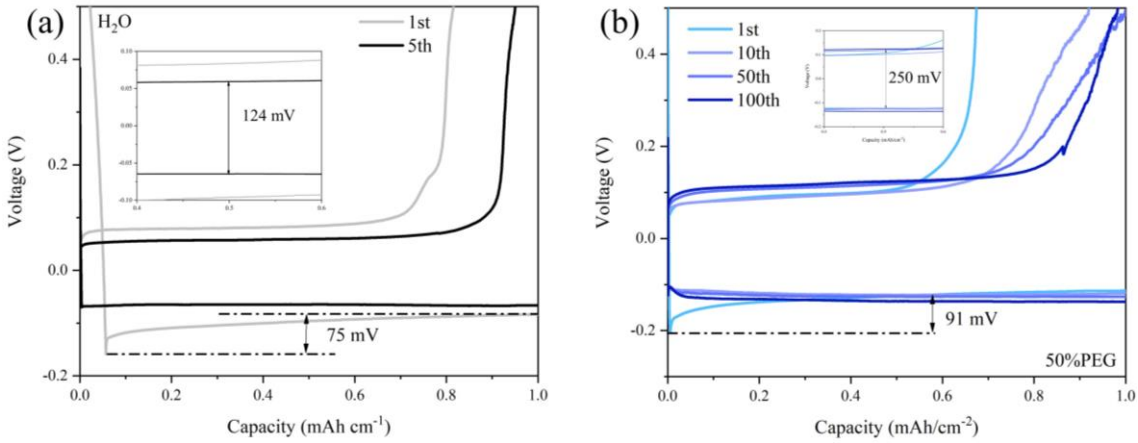

Figure 15 Charge and discharge curves of Ti_3C_2||Zn half-cell in (a) H_2O and (b) 50% PEG electrolyte at 1mA cm^{-2}

The charge and discharge curves of the Ti_3C_2||Zn half-cell at 1mA cm^{-2}, 1mAh cm^{-2} in different electrolytes are shown in Figure 15 (a) and (b). The charge and discharge curve in both 50% PEG and H_2O electrolyte exhibit stable charge and discharge plateau, which demonstrate the occrence of stripping/plating process of zinc metal on the Ti_3C_2 surface. Additionally, both electrolytes show a significant voltage spike during the first cycle of deposition, attributed to the nucleation process of Zn on the Ti_3C_2 surface as mentioned in chapter 1.1.1. [14]

The difference in plateau overpotentials is 124 mV for the H_2O electrolyte, while for the 50% PEG electrolyte, it is 250 mV, which is twice as large, likely due to the low conductivity of 50% PEG. Additionally, the nucleation overpotential of zinc deposition in H_2O electrolyte is 75 mV, while in 50% PEG electrolyte, it is 91 mV. According to formula (11), a higher nucleation overpotential typically results in smaller grain size. [10]

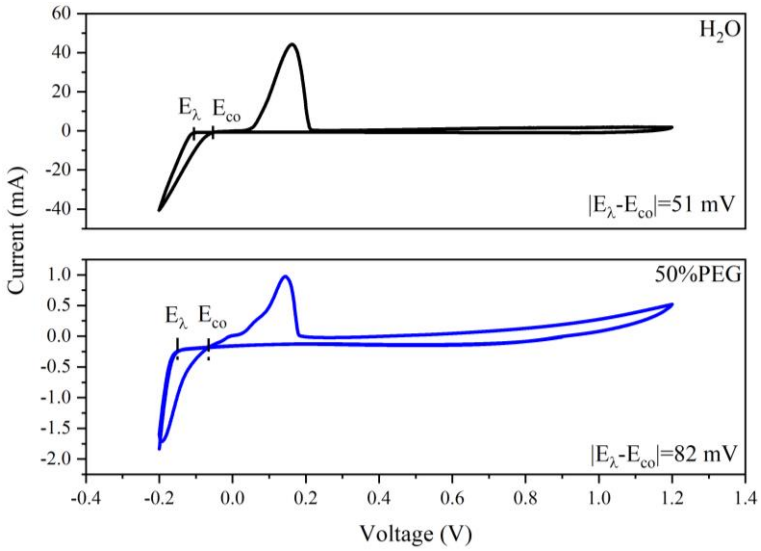

Figure 16 CV curve of Ti_3C_2||Zn half-cell in (a) H_2O and (b) 50% PEG electrolyte

The deposition behavior of zinc on the Ti_3C_2 surface is also characterized by CV in the voltage range of -0.2 to 1.2 V with a scan rate of 2 mV/s (figure 16 (a) and (b)). Similar to the typical zinc deposition images mentioned in Chapter 2.3.4, Ti_3C_2 anode in the H_2O and 50% PEG electrolyte exhibit similar CV shapes. During a negative scan, a more negative potential (switching potential, E_λ) is often required to generate current, which is associated with the initial nucleation process. During the positive scan, an intersection with the negative scan curve can be seen. The potential at this intersection is called the crossover potential (E_{co}), which reflects the equilibrium potential. [105] Continuing the positive scan results in the appearance of a zinc oxidation peak, representing the conversion of zinc metal to zinc ions.

The CV curve of zinc deposition in H_2O and 50%PEG electrolyte exhibit the same crossover potential, indicating the same Zn^{2+}/Zn equilibrium potential. This is because, in the same electrochemical reaction at the same temperature and pressure, the equilibrium potential is only determined by the concentrations of the oxidized and reduced species. [110]

However, the CV curve of zinc deposition in H_2O and 50%PEG electrolyte show different switching potentials. The difference between the switching potential and the crossover potential represent an overpotential of 51 mV and 82 mV, respectively. The larger overpotential for 50%PEG may result from the lower ionic conductivity, which is consistent with the conclusions drawn from the charge and discharge curves.

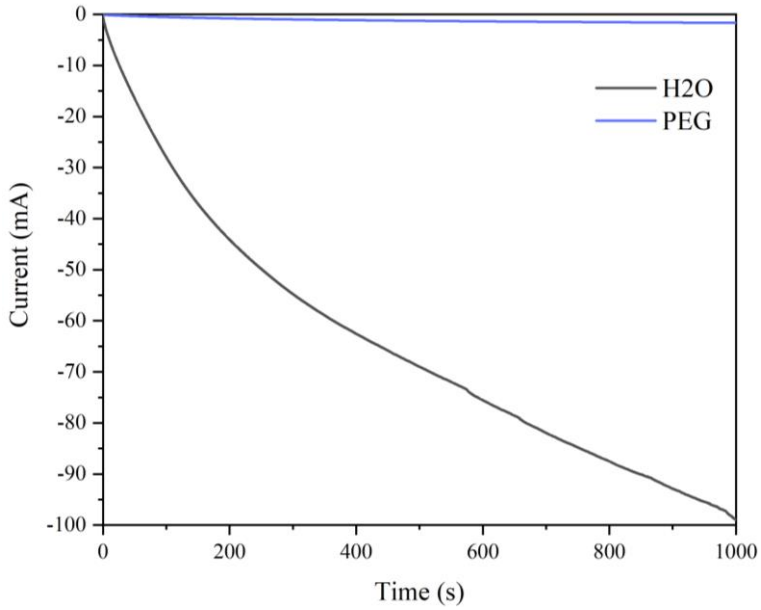

Figure 17 Chronoamperometry curve of Zn||Zn symmetric cell in different electrolyte

To understand the effect of PEG on the subsequent growth steps of zinc, which has significant impact on the deposition behavior, the CA test is conduct. As shown in Figure 17, a voltage of -150 mV was applied to the Zn||Zn symmetric cell, and the current-time response was detected to reflect the nucleation and growth process of Zn on the Zn surface. As can be seen from figure 17, the current of Ti_3C_2 anode in the 50% PEG electrolyte hardly changed and remained stable at around 3 mA. However, the current of Ti_3C_2 anode in H_2O electrolyte continued to rise to 100 mA within 1000 s.

In the H_2O electrolyte, the current density continuously increased under the applied constant voltage. According to the Bewick, Fleischman, and Thirsk (BFT) model described in Chapter 1.1.1, this continuously increasing current density corresponds to the control of 2D diffusion. (Equation (3) and (4)) [11], [16] The 2D diffusion process describes a growth mode of zinc grains, where zinc atoms adsorbed on the zinc anode surface migrate along the zinc anode to find energetically favorable sites. However, the larger grains formed by this 2D diffusion aggregation process tend to attract more adsorbed zinc atoms due to the “tip effect”, leading to the formation of dendrites. Some studies have also pointed out that the continuous increase in current under constant voltage control corresponds to a continuous increase in the “effective surface area” of the electrode[19], [20], further indicating more severe dendrite growth.

In contrast, the current of Ti_3C_2 in 50% PEG electrolyte remained stable at 3 mA under an applied potential of -150 mV. This stability aligns with 3D diffusion behavior as described by the Armstrong, Fleischmann, and Thirsk (AFT) model (Equation 7). [19], [20] Different from 2D diffusion, the zinc grain growth under 3D diffusion control is determined by the concentration gradient of zinc atoms in the electrolyte near the zinc grains. This 3D diffusion control mode may contribute to a more uniform deposition due to relatively uniform gradient of zinc atom across the surfaces. The addition of PEG resulted in a transition of grain growth mode from 2D diffusion control to 3D diffusion control. This shift can be attributed to the parallel adsorption facilitated by PEG [96], which restricts the free diffusion of zinc atoms on the surface of the zinc anode. Additionally, the consistent and lower current density suggests a smaller "effective surface area," likely due to PEG adsorption inhibiting the 2D diffusion of zinc atoms.[96]

In summary, the zinc deposition process was investigated using GCD and CV curves. Stable zinc plating/stripping behavior and nearly unchanged equilibrium potential were observed. Additionally, GCD highlighted the higher nucleation overpotential and plateau overpotential of zinc in the 50% PEG electrolyte during deposition on the Ti_3C_2 surface. Furthermore, CA confirmed distinct zinc grain growth modes in 50% PEG and H_2O electrolytes, where zinc grain growth in the 50% PEG electrolyte was governed by 3D diffusion and had a smaller effective surface area, which may contribute to fewer dendrites and smoother interfaces during deposition.

3.2.2 Overall morphology and texture of zinc deposited on Ti_3C_2 surface

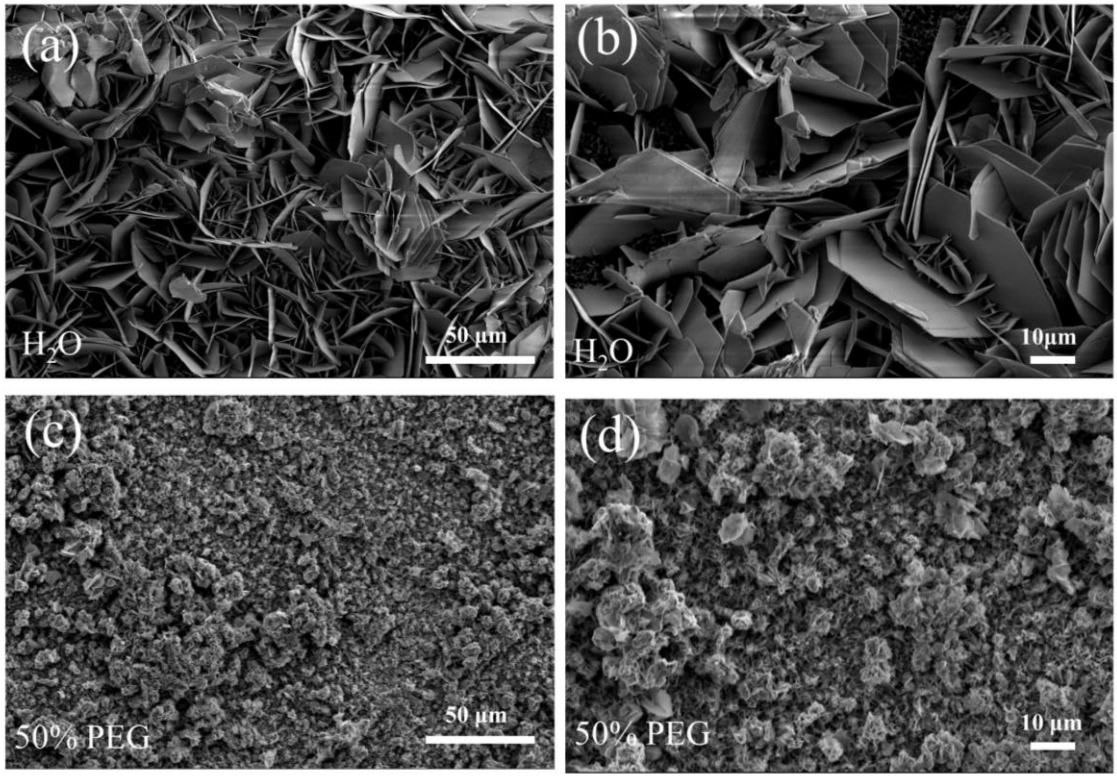

Figure 18 SEM images of Zn platting on Ti_3C_2 in (a)(b) H_2O and (c)(d) 50% PEG

To verify the results of the previous electrochemical experiments, SEM measurements were conducted to observe the morphology of zinc deposited on the Ti_3C_2 surface at a constant current of 1 mA cm^{-2} with a capacity of 1mAh cm^{-2} in a beaker cell.

Figure 18 (a) and (b) reveal that zinc deposition on the Ti_3C_2 surface in the H_2O electrolyte results in large flake structures (10-50 μm) and protrusions. This hexagonal flake structure arises from the intrinsic hexagonal close-packed (HCP) crystal structure of zinc metal. In addition, the formation of complete and well-defined hexagonal grains can be attributed to the intense 2D diffusion process during grain growth, as indicated by the CA test results. Specifically, during the zinc grain growth process under 2D diffusion control, the zinc atoms adsorbed on the zinc surface tend to migrate to the zinc nucleus by diffusion, leading to uneven zinc deposition and more complete grain growth. In contrast, during the zinc grain growth process under 3D diffusion control, the growth of zinc grains is limited by

the zinc atom concentration gradient near the grain surface. This concentration gradient is relatively uniform across different surfaces, resulting in more uniform deposition. [11]

In contrast, Figure 18 (c) and (d) show a different morphology for zinc deposited on the Ti_3C_2 surface in the 50% PEG electrolyte. More compact and smaller grains tend to agglomerate, forming a denser surface. This phenomenon aligns with the restricted 2D diffusion process observed in the CA test. However, poor conductivity may lead to concentration polarization, resulting in a certain degree of dendrite formation, as shown in Figure 18(d).

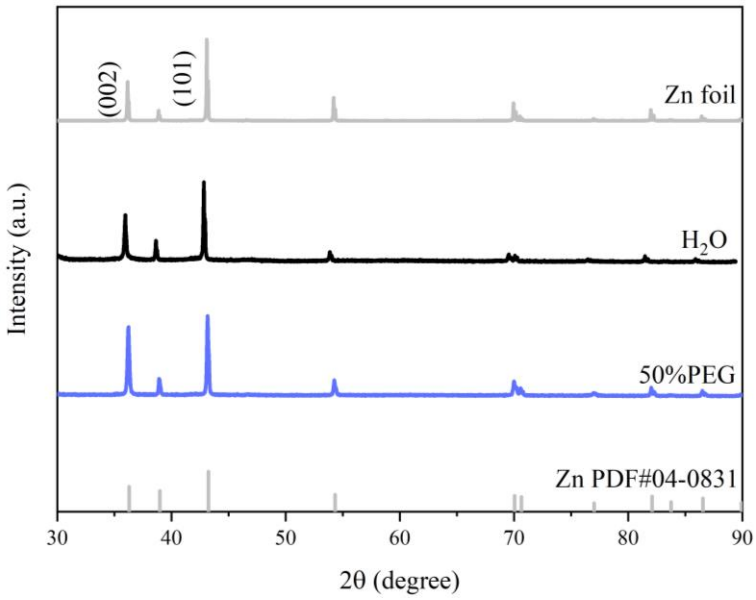

Figure 19 XRD patten of Ti_3C_2 Zinc-free anode after cycles in H_2O and 50% PEG

The Ti_3C_2||Zn half-cell was cycled 12 times in different electrolytes, then disassembled for XRD analysis to examine the structure of deposited Zn on Ti_3C_2 surface. The presence of zinc on the Ti_3C_2 surface was confirmed in the range of 30-90 degrees (reference PDF#04-0831) for different electrolytes.

Furthermore, it was observed that after the addition of PEG, the intensity ratio (002)/(101) increased from 0.59 in water to 0.86 in 50% PEG. The (002) crystal orientation corresponds to the direction along the substrate. Generally, a higher (002)/(101) ratio is believed to be advantageous for suppressing dendrite growth.

In this section, the electrochemical process of zinc deposition on the Ti_3C_2 surface was initially studied using GCD and CV, confirming the occurrence of zinc deposition. Upon adding PEG to the electrolyte, zinc deposition exhibited higher plateau and nucleation overpotentials. CA was then employed to delve deeper into the subsequent zinc grain growth process, revealing that PEG effectively inhibits 2D diffusion. Subsequently, SEM and XRD analyses were conducted to validate the electrochemical results. XRD analysis further confirmed that the addition of PEG promoted the deposition of zinc with more (002) oriented crystals on the Ti_3C_2 surface, facilitating more uniform deposition. SEM images demonstrated that the addition of PEG in the electrolyte altered the morphology of zinc deposited on the Ti_3C_2 surface from large flakes to smaller agglomerates, which aligns with the above test. In short, the deposition of Zn on the Ti_3C_2 anode surface in 50% PEG electrolyte showed a more uniform

deposition than that in H_2O electrolyte. However, dendrites were still generated, which may be attributed to the severe concentration polarization caused by the poor ionic conductivity of 50% PEG.

3.3 Electrochemical Performance of Ti_3C_2 Zn-free anode

After analyzing the effects of different electrolytes on the hydrogen evolution reaction and deposition behavior, Ti_3C_2||Zn half-cells were assembled to test the cycle life, coulombic efficiency, and rate performance.

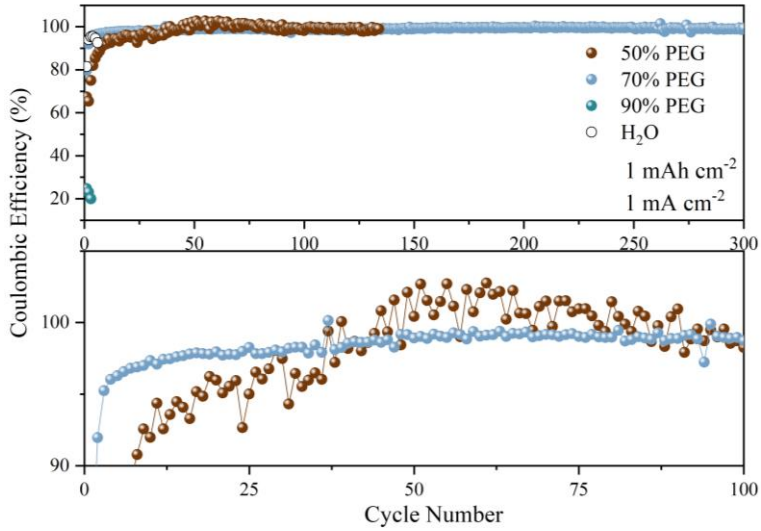

Figure 20 Coulombic efficiency and cycle life of Ti_3C_2||Zn half-cell in different electrolyte systems

GCD was used to test the cycle life and coulombic efficiency at 1mA cm^{-2} and 1mAh cm^{-2} in different electrolytes. As shown in Figure 20, we first characterized the coulombic efficiency and cycle life of Ti_3C_2 zinc-free anode in 50% PEG electrolyte and. Compared with the 92.25% coulombic efficiency and 14h life of the H_2O group, Ti_3C_2 zinc-free anode in 50%PEG electrolyte has a coulombic efficiency of 97.67% and a longer cycle life of 268 h. In order to further improve the performance of the PEG system, we optimized the ratio of PEG:H_2O. Among them, the Ti_3C_2 zinc-free anode demonstrated the highest coulombic efficiency of 98.95% and a long cycle life of 600 hours in 70% PEG electrolyte. However, it could hardly be cycled in 90% PEG electrolyte due to poor kinetics. Additionally, by comparing the magnified images, it can be observed that the coulombic efficiency of the Ti_3C_2 zinc-free anode in 70% PEG showed small fluctuations between cycles (~2%), whereas this fluctuation was particularly noticeable in the 50% PEG electrolyte group (~5%).

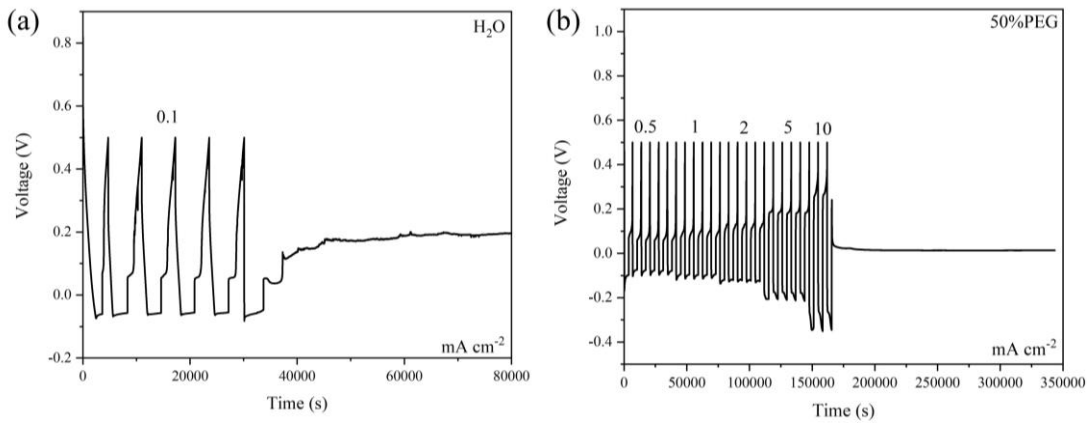

Figure 21 Rate performance of Ti_3C_2 zinc free anode in (a) H_2O and (b) 50%PEG

The same Ti_3C_2||Zn half-cell was assembled to test the rate performance at different current densities. The Ti_3C_2 anode failed quickly in H_2O electrolyte, whereas it could tolerate up to 10 mA cm^{-2} and 10 mAh cm^{-2} in 50% PEG electrolyte.

In summary, the inclusion of PEG disrupts the hydrogen bond network, thereby inhibiting the HER. Additionally, PEG promotes orientational zinc growth and hinders 2D diffusion, leading to uniform zinc deposition. These factors improve coulombic efficiency and notably prolong cycle life in the PEG electrolyte system. By optimizing PEG concentration to 70%, coulombic efficiency reaches 98.95% (a 6.7% enhancement), and cycle life extends to 600 hours (a 42-fold increase).

Although the use of PEG-based electrolytes can effectively improve the coulombic efficiency and cycle life of Ti_3C_2 anodes, the performance improvement is still limited by the low ionic conductivity of PEG. Many phenomena possibly derived from its poor mass transfer in electrolyte introduced by the low ionic conductivity of PEG, such as higher plateau overpotentials after adding PEG and half-cells that cannot be cycled at high concentrations. This poor mass transfer may lead to more severe concentration polarization, resulting in dendrite growth, as seen in figure 18. Therefore, to avoid the poor ionic conductivity and high viscosity of long-chain polymers, another small molecule with a nucleophilic group will be added in electrolyte as a co-solvent for further attempts.

4 Weakly solvating Zn-based aqueous electrolyte enabled by IPA cosolvent

As a common solvent, the electrochemical performance of isopropanol (IPA) has been validated in various fields, including lithium-ion batteries[111], zinc-ion batteries[112], fuel cells[113], and electrocatalysis[114]. However, its compatibility with Ti_3C_2 zinc-free anodes has rarely been studied.

In this chapter, IPA will be added to the aqueous electrolyte as a co-solvent. Firstly, the electrolyte structure will be characterized using FTIR and Raman techniques to illustrate the change of chemical structure. Subsequently, the change of hydrogen evolution behavior will be confirmed by LSV measurements. Additionally, the zinc deposition behavior will be characterized by GCD, CV and CA, with the surface morphology verified by SEM and XRD. Following this, the interfacial structure between Ti_3C_2 and the electrolyte will be explored by XPS analysis. Finally, the coulombic efficiency and cycle life are characterized by GCD to verify the contribution of all the above aspects to the stability for Ti_3C_2 Zinc-free anode.

4.1 Formation of weak solvation structure

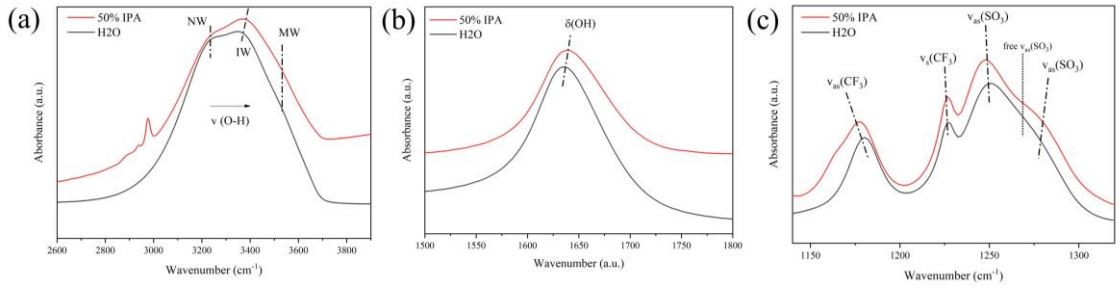

Figure 22 FTIR spectra of different electrolytes in different wavenumbers

To understand the effect of adding IPA on the chemical structure of the electrolyte, FTIR and Raman spectroscopy were performed. The electrolyte system in which 1M $Zn(OTF)_2$ is dissolved in H_2O is denoted as H_2O. The electrolyte system in which 1M $Zn(OTF)_2$ is dissolved in a solvent with a volume ratio of IPA:H_2O=1:1 is denoted as 50%IPA. All electrolytes contain 1M $Zn(OTF)_2$.

As discussed in Chapter 1.4.1, the addition of a cosolvent will affect the hydrogen bond network between the H_2O molecules. The figure 22 (a) shows a decrease in the intensity of NW, indicating that the addition of IPA effectively disrupts the hydrogen bond network. This effect may be attributed to the strong nucleophilic oxygen atoms in IPA can compete with H_2O molecules for coordination, replacing part of the water in the hydrogen bond network. At the same time, the IW peak and O-H bending vibration (figure 22 (b)) undergoes a blue shift. This may also be due to the oxygen in IPA forming coordination bonds, thereby altering the coordination environment of water. [45] [109]

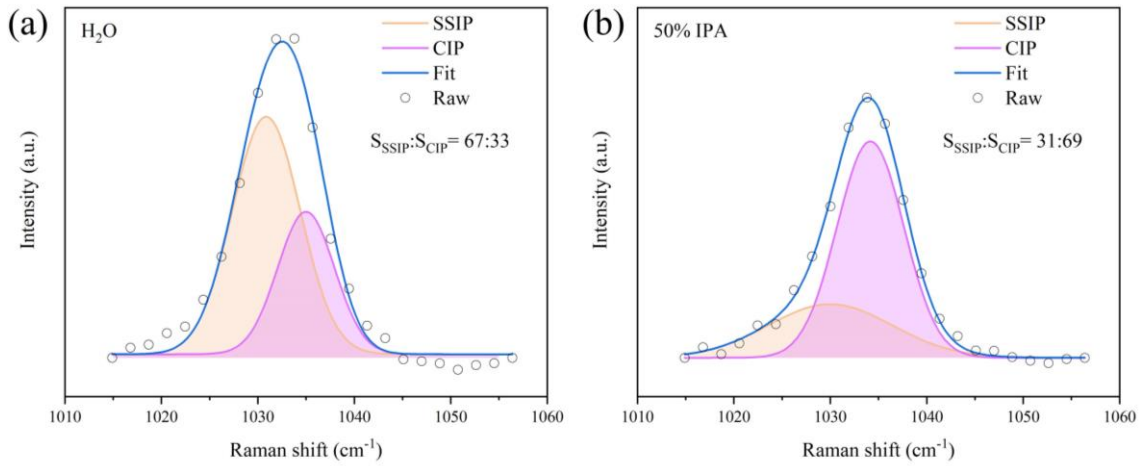

Figure 22 Raman spectra in the region from 1015 to 1055 cm^{-1} for (a) H_2O and (b) 50% IPA

Furthermore, IPA also influences the solvation structure and the interaction between OTF^- anions and Zn^{2+} ions. As shown in Figure 22 (c), the $SO_3(V_{as}SO_3)$ asymmetric vibration at 1270 cm^{-1} represents the "free OTF^- anions" that are not involved in ion pairs or aggregates. With the addition of IPA, the intensity of "free OTF^- anions" decreases, and the peak splits into two peaks at 1282-1317 cm^{-1} and 1237-1248 cm^{-1}. This indicates a reduction in free OTF^- anions and enhanced coordination between Zn^{2+} and OTF^-. [115] The fitting of the Raman spectrum (figure 23 (a) and (b)) also supports this point. The peaks of SO_3 symmetric vibration $V_{as}SO_3$ at 1015 cm^{-1} to 1055 cm^{-1} were fitted separately. Solvent-separated ion pairs (SSIP) near 1030 cm^{-1} and contact ion pairs (CIP) near 1035 cm^{-1} were identified. SSIP represents the symmetric vibration of SO_3 in anion-cation pairs separated by solvent, while CIP represents the symmetric vibration of SO_3 in contacting anion-cation pairs. After adding IPA, the proportion of CIP increased significantly from 33% to 67%, indicating that IPA promotes more Zn-OTF^- contacts.[91], [115] As mentioned in Chapter 1.4.2, a low dielectric constant often indicates lower polarity and weaker solubility. Herein, the lower dielectric constant of IPA (19.91) compared to H_2O (80) effectively reduces the solvent's solubility, and thereby enhances the contact between OTF^- anions and Zn^{2+} cations (also known as weak solvation structure). [116]

In short, this chapter uses FTIR and Raman spectroscopy to prove that (1) the addition of IPA has the ability to break the original hydrogen bond network, and (2) the addition of IPA strengthens the Zn^{2+}-OTF^- contact, which is considered indicative of the formation of a weakly solvated structure.

4.2 Bulk electrolyte properties

After the chemical structure changes, the conductivity and electrochemical stability of the bulk electrolyte will be discussed in this section.

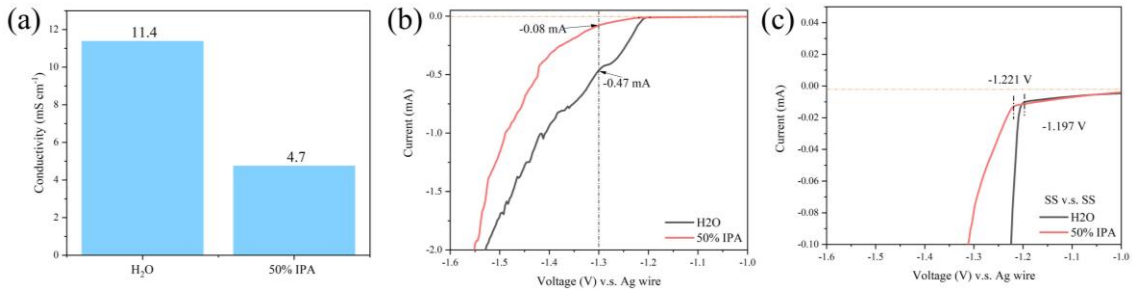

Figure 24 (a) conductivity of different electrolyte. (b) and (c) LSV curve for different electrolyte.

As shown in Figure 24 (a), the conductivity of the electrolyte decreased from 11.4 mS cm^{-1} to 4.7 mS cm^{-1} after adding IPA. This may be attributed to the higher viscosity of IPA (2.37 mPa • s at 20℃) and lower dielectric constant compared (19) to H_2O (1.0016 mPa • s and 80 at 20℃).[117] Lower conductivity may lead to an increase in the overpotential, as will be observed in Chapters 4.4.

The hydrogen evolution reaction of the electrolyte is characterized by linear sweep voltammetry (LSV). As shown in Figure 24 (b), at a potential of -1.3 V vs Ag wire, the current of the H_2O group was -0.47 mA, while the current of 50% IPA was -0.08 mA. This indicates that the yield of hydrogen evolution is suppressed. Figure 24 (c) presents an enlarged LSV image, highlighting the starting potential of hydrogen evolution. The starting potential of HER in pure water is -1.197 V, while in the 50% IPA electrolyte, it is more negative at -1.221 V. The addition of IPA shifts the hydrogen evolution potential of the electrolyte negatively by 24 mV.

The inhibition of hydrogen evolution yield and hydrogen evolution potential may arise from two factors: (1) As introduced in Chapter 1.4.2, the majority of the hydrogen evolution reaction originates from the water in the solvation structure. [84] A decrease in solvated water leads to a reduction in hydrogen evolution. In this work, the OTF^- anions compete with H_2O to enter the solvation sheath of the zinc ion, thereby reducing the H_2O content in the solvation structure and suppressing the HER. This phenomenon can be confirmed by the increase in CIP ratio in Raman measurement and the decrease in "free OTF^-" in FTIR. in Chapter 4.1. (2) As mentioned in Chapter 1.4.1, the oxygen atom in the water molecule forms a covalent bond with the hydrogen atom inside the molecule and forms a hydrogen bond with the hydrogen atom of another water molecule. When the hydrogen bond between the H_2O is broken, the OH covalent bond inside the H_2O is strengthened. [80] In this work, the nucleophilic oxygen atoms in IPA disrupt the hydrogen bond network, thereby strengthening the OH covalent bond and suppressing the HER. This phenomenon can be confirmed by the weakening of the NW peak intensity in FTIR in chapter 4.1.

4.3 Deposition behavior

Next, we investigate the Zn plating/stripping process on Ti_3C_2 in H_2O and 50%IPA electrolytes. The electrochemical methods such as GCD, CV and CA are used to characterize the behavior of zinc deposition. SEM and XRD were performed to verify the morphology and orientation of the zinc deposition.

4.3.1 Deposition of zinc on Ti_3C_2 surface

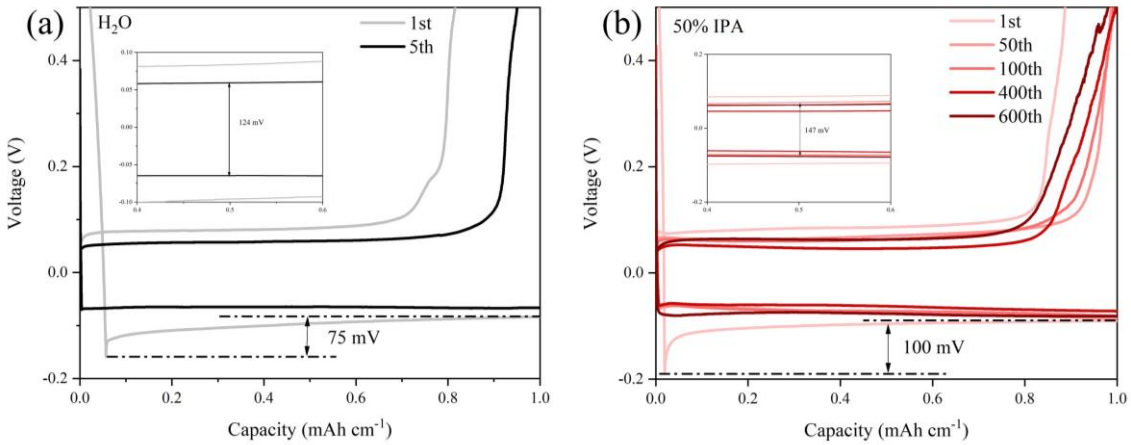

Figure 25 Charge and discharge curves of Ti_3C_2||Zn half-cell in (a) H_2O and (b) 50% IPA electrolyte at 1mA cm^{-2}

The charge and discharge curves of the Ti_3C_2||Zn half-cell at 1mA cm^{-2}, 1mAh cm^{-2} in different electrolyte are shown in Figure 25 (a) and (b). Both H_2O and 50% IPA exhibit stable charge and discharge plateau, which demonstrate the stable stripping/plating process of zinc metal on the Ti_3C_2 surface. Additionally, both electrolytes show a significant voltage spike during the first cycle of deposition, attributed to the nucleation process of Zn on the Ti_3C_2 surface as mentioned in chapter 1.1.1. [14]

The difference in plateau overpotentials is 124 mV for the H_2O electrolyte, while 50% IPA shows a slightly higher value of 147 mV, possibly due to the lower conductivity of 50% IPA. Furthermore, the nucleation overpotential for H_2O is 75 mV, whereas 50% IPA has a higher nucleation overpotential of 100 mV. According to formula (11), a higher nucleation overpotential typically results in smaller grains, and thereby leading to a smoother surface. [10]

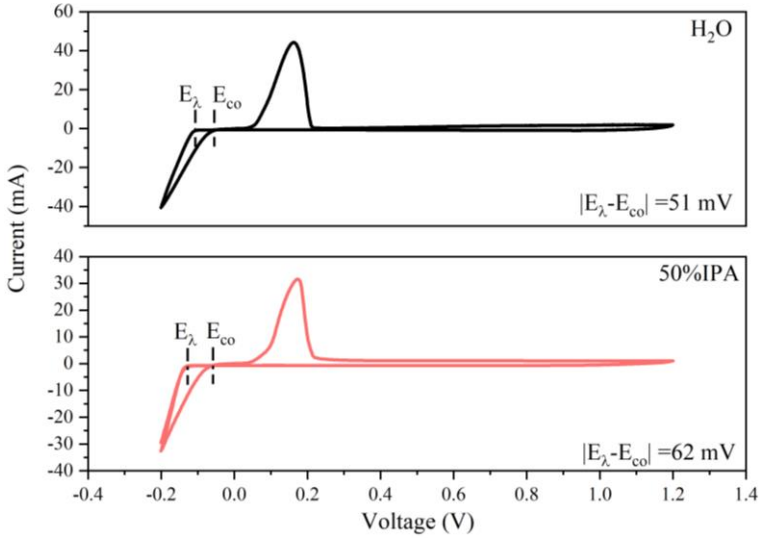

Figure 26 CV curve of Ti_3C_2||Zn half-cell in (a) H_2O and (b) 50% IPA electrolyte

CV was also performed to study the deposition process in the range of −0.2 V–1.2 V at a scan rate of 2 mV/s. Similar to what was mentioned before, Zinc deposition in both electrolytes exhibited similar crossover potentials, which may be attributed to the same equilibrium potential. However, H_2O and 50% IPA show different switch potentials. The difference between the switch potential and the crossover potential represents an overpotential of 51 mV (H_2O) and 62 mV (50% IPA). The slightly larger overpotential for 50% IPA is consistent with the conclusions drawn from the charge and discharge curves.

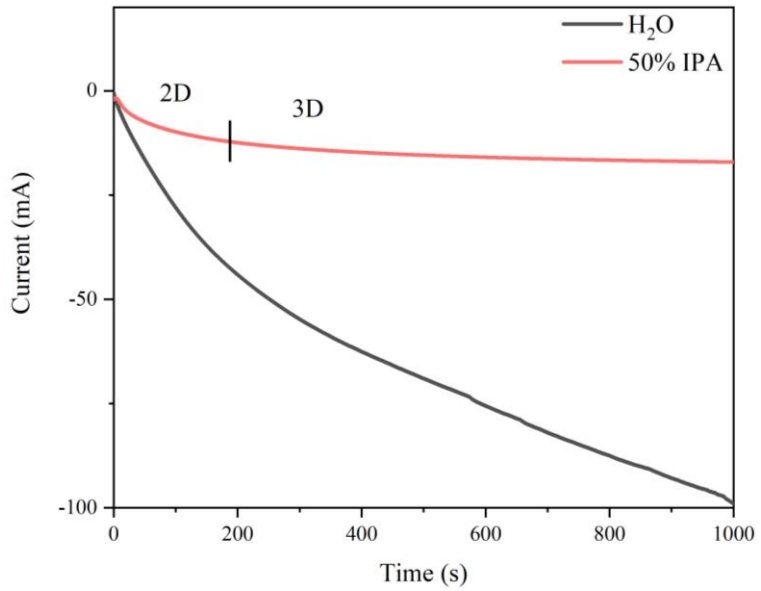

Figure 27 Chronoamperometry curve of Zn||Zn symmetric cell in different electrolyte

To understand the influence of the electrolytes on Zn diffusion process, which has significant impact on the deposition behavior, the CA test is conduct. As shown in Figure 27, a voltage of -150 mV was applied to the Zn||Zn symmetric cell, and the current-time response was detected to reflect the

nucleation and growth process of Zn on the Zn surface. It was observed that both the H_2O and 50% IPA electrolyte groups exhibited a certain degree of current drop. However, 50% IPA maintained a stable current of 15 mA after 200 s, while H_2O continued to rise to 100 mA within 1000 s.

As we mentioned before, in the H_2O electrolyte, the current density continuously increased under the applied constant voltage. According to the Bewick, Fleischman, and Thirsk (BFT) model described in Chapter 1.1.1, this continuously increasing current density corresponds to the control of 2D diffusion (Equation (3) and (4)) [11], [16], indicating stronger grain growth. Some studies have also pointed out that the continuous increase in current under constant voltage control corresponds to a continuous increase in the “effective surface area” of the electrode[19], [20], further indicating more severe dendrite growth.

In contrast, after a short period of 2D diffusion control (200 s), the 50% IPA group exhibited a long-term stable current (15 mA). This satisfies the description of 3D diffusion by the Armstrong, Fleischmann, and Thirsk (AFT) model (Equation (7)) [19], [20], suggesting that zinc deposition is controlled by the concentration gradient of zinc in the electrolyte, leading to more uniform zinc growth. Similarly, the constant current also indicates that the “effective surface area” of the electrode remains unchanged, demonstrating that dendrite growth is suppressed. [19], [20]

In general, GCD, CV, and CA indicate that the presence of IPA slightly increases the nucleation overpotential in the first stage. Simultaneously, the addition of IPA limits two-dimensional diffusion and the increase in the effective surface area.

4.3.2 Overall morphology and texture of zinc deposited on Ti_3C_2 surface

To further understand the Zn deposition behavior on $Ti_3C_2T_x$ in 50%IPA electrolytes, SEM and XRD were performed to examine the morphology and texture of Zn deposited on Ti_3C_2 surface.

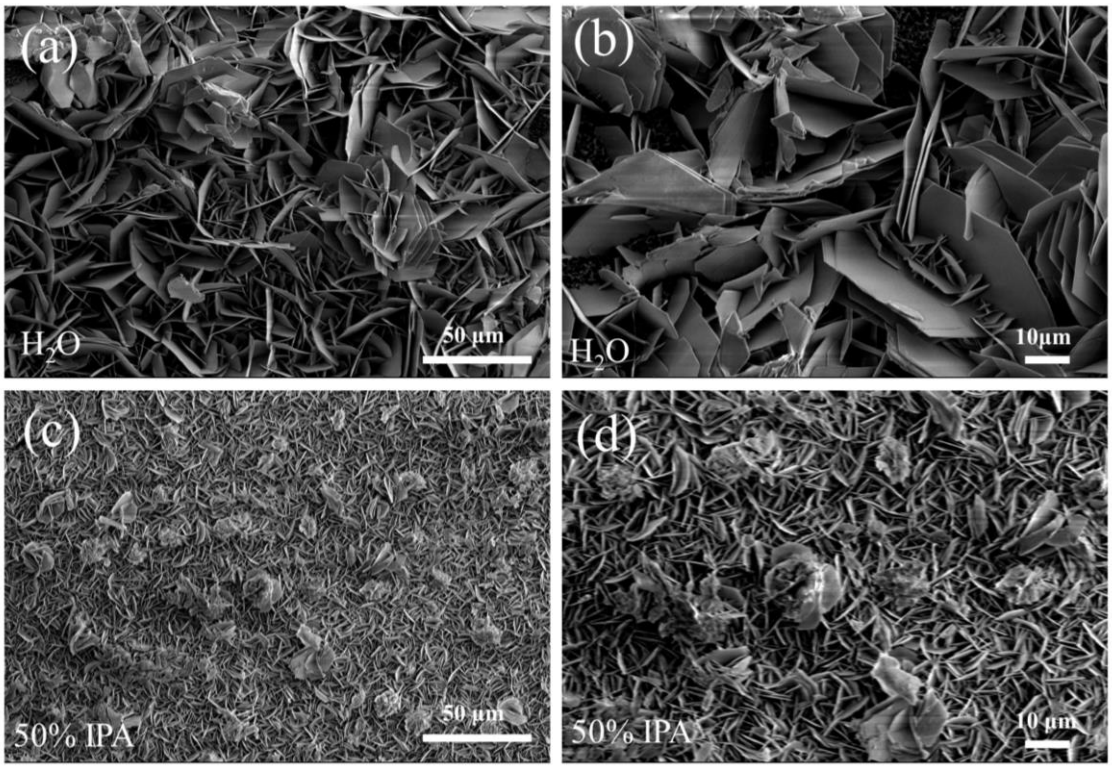

Figure 28 SEM images of Zn platting on Ti_3C_2 in (a)(b) H_2O and (c)(d) 50% IPA

Figure 28 shows the morphology Zn on the surface of Ti_3C_2 Zn-free anode (with 1 mAh cm^{-2} Zn deposited at 1 mA cm^{-2}) after 12 cycles in H_2O(a)(b) and 50% IPA electrolytes (c)(d).

The plated Zn exhibit similar hexagonal flake structures in both H_2O and 50% IPA, originating from the intrinsic HCP crystal structure of Zn.[118] However, the deposited Zn in H_2O electrolyte displayed dendritic morphology as large (10-50 μm) Zn flakes and non-uniform protrusions are observed. This non-uniform growth may be related to the strong 2D diffusion observed in the CA test. In contrast, the deposited Zn in 50%IPA electrolyte shows a smaller grain size (less than 10 μm) and a more uniform and flatter surface, possibly due to the limitation of 2D diffusion and smaller "effective surface area", thereby mitigating the dendrite growth.

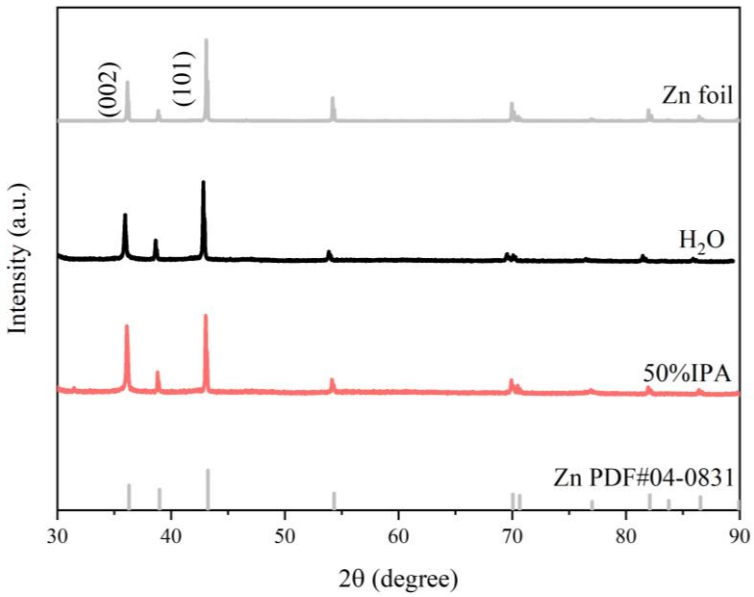

Figure 29 XRD patten of Ti_3C_2 Zinc-free anode after cycles in H_2O and 50%IPA

The XRD patterns was then used to characterize the texture of Zn on Ti_3C_2 surface. First, peaks corresponding to zinc were observed in the range of 30°-90°, proving that zinc was deposited on the Ti_3C_2 surface. According to PDF #040831, the (101) crystal plane, which is angled relative to the plane of the zinc metal, is dominant. The intensity ratio of peak (002) and (101) of zinc on the Ti_3C_2 surface cycled in the H_2O electrolyte is 0.59. In contrast, this ratio increases to 0.87 for 50% IPA, indicating that in 50% IPA electrolyte, the plated zinc has more (002) crystal planes growing parallel to the Ti_3C_2 plane. Corresponding to SEM observations, although the (101) crystal plane remains dominant (as shown in figure 28), the preferred growth along (002) crystal planes may lead to less dendritic behavior .[119]

In this section, the two stages of Zn deposition on the Ti_3C_2 surface and the final morphology and texture are mainly examined. The preferred growth along (002) (confirmed by XRD) as well as the limited 2D diffusion after the addition of IPA is beneficial for the more uniform deposition of Zn.. It is worth noting that the uniform deposition may also be related to OTF^- entering the solvation structure to help form the SEI. [120]

4.4 Formation of SEI

Typically, weakly solvated structures tend to form a stable SEI facilitated by anions in the solvation sheath. [120] Therefore, in this section, XPS was performed to verify the existence and composition of SEI.

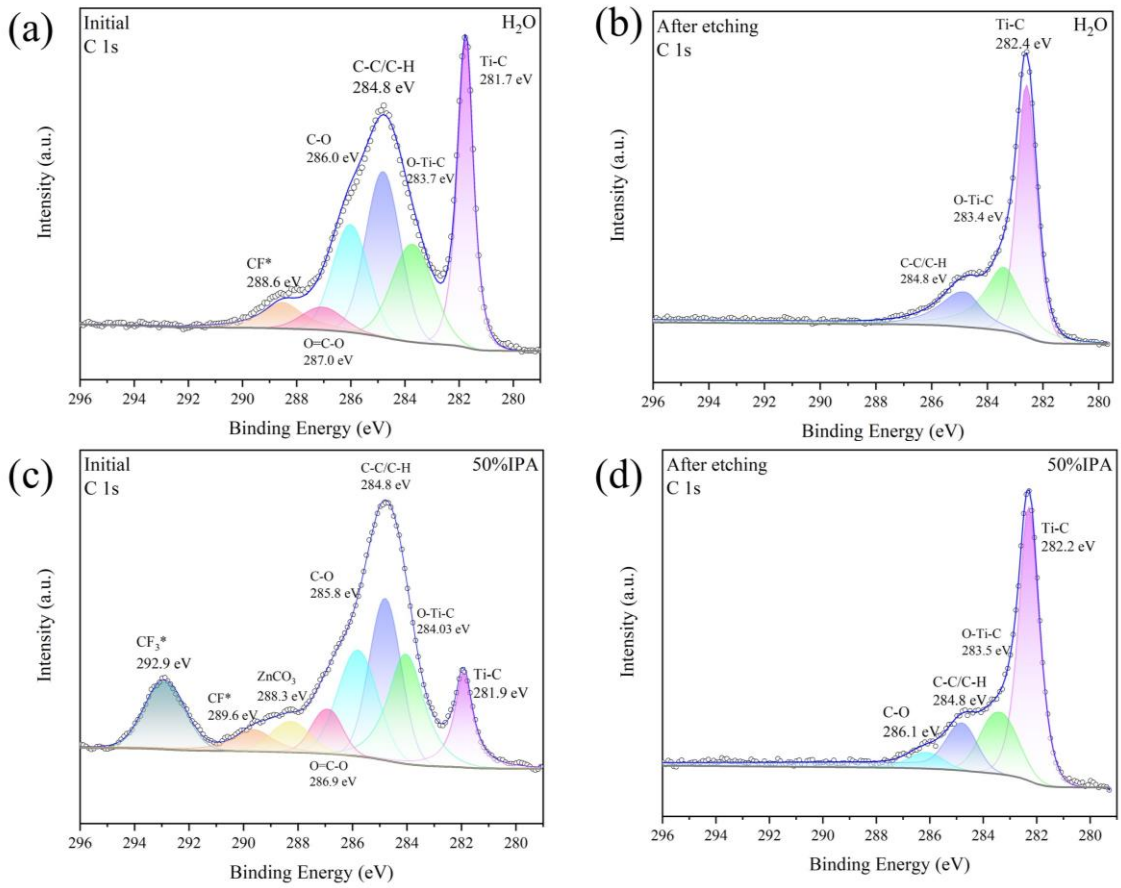

Figure 30 the deconvoluted XPS spectra. Panels (a) and (b) show the C 1s spectra of the H_2O group before and after etching, respectively. Panels (c) and (d) display the C 1s spectra of the 50% IPA group before and after etching, respectively.

Figure 30 (a) (b) (c) (d) showed the C 1s spectrum of Zn-deposited $Ti_3C_2T_x$ in different electrolytes. In H_2O electrolyte before etching, the C 1 s result (figure 30 (a)) reveals peaks: Ti-C (281.7 eV), O-Ti-C (283.7 eV), C-C/C-H (284.8 eV), C-O (286.0 eV), O=C-O (287.0 eV), CF* (288.6 eV). The strong Ti-C signal is attributed to the Ti_3C_2 bulk structure, suggesting a directly exposed interface with minimal SEI formation. In contrast, in 50% IPA electrolyte before etching, the C 1s spectrum shows stronger organic signals and weaker Ti-C peaks before etching, indicating the possibility of forming SEI layer. The presence of strong CF_3 (293.0 eV) peaks and $ZnCO_3$ (288.3 eV) confirms the formation of SEI, likely derived from the OTF^- anions incorporated into the solvation sheath. After the etching process, in the 50% IPA electrolyte, the spectrum resembles that of the H_2O electrolyte, further verifying the presence of an SEI layer confined to the surface. [121], [122], [123], [124]

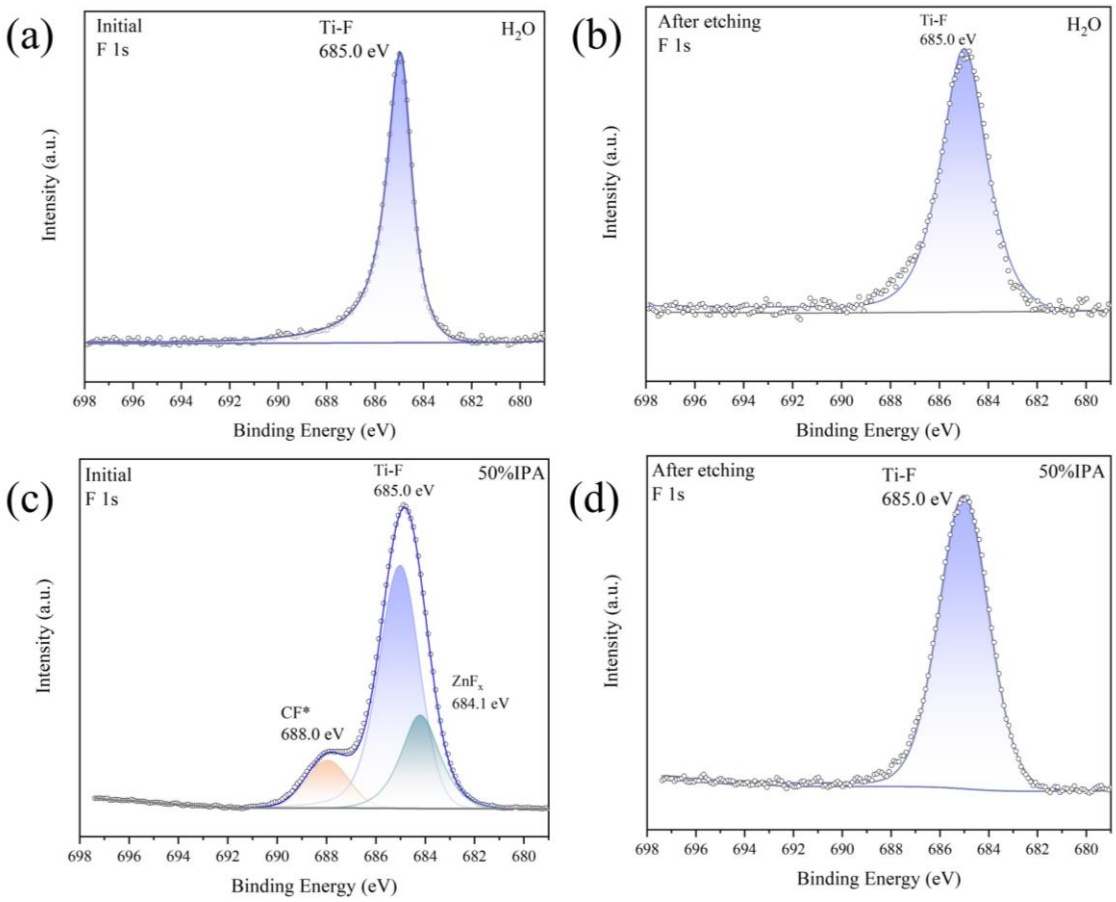

Figure 31 the deconvoluted XPS spectra. Panels (a) and (b) illustrate the F 1s spectra of the H_2O group before and after etching, respectively. Panels (c) and (d) depict the F 1s spectra of the 50% IPA group before and after etching, respectively.

Comparing the F 1s spectra (figure 31 (a) (b) (c) (d)), the Zn-deposited $Ti_3C_2T_x$ in both H_2O and 50% IPA electrolytes exhibit Ti-F peaks (685.0 eV).[124], [125] However, in the initial 50%IPA electrolyte, we also observed the peak of CF*(688.0 eV) and ZnF_x(684.8 eV), which once again verified the formation of SEI.

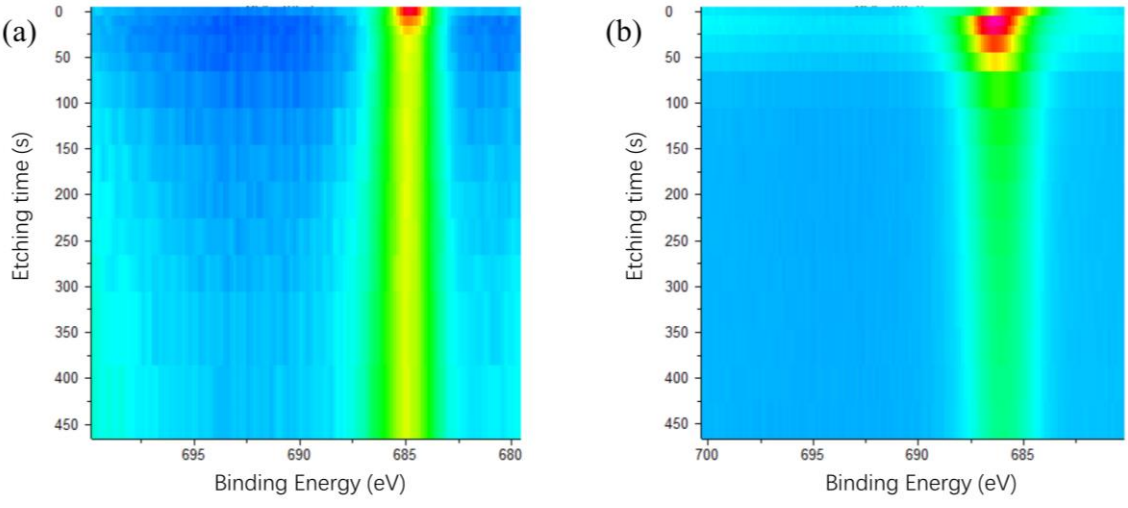

Figure 32 XPS spectra for F 1s at different etching times, where (a) H_2O group (b) 50%IPA group.

With the help of depth profile images (figure 32 (a) (b)), the presence of the ZnF_x peak on the surface becomes more evident. The Ti-F peak in the F 1s depth profile in the H_2O electroyte remains constant. In contrast, the peak position shifts significantly to the left in the 50% IPA electrolyte, which means the disappearance of ZnF_x and the dominance of Ti-F in the bulk Ti_3C_2.[125]

In conclusion, the XPS spectra confirmed the presence of a SEI layer with $ZnCO_3$, ZnF_x and Fluorine-rich (CF* and CF_3*) organic compounds on the surface of Ti_3C_2 anode in 50%IPA electrolyte, likely resulting from the incorporation of OTF^- anions into the solvation sheath. This SEI layer may help to guide the ion distribution, leading to a uniform deposition of Zn, thereby helping to stabilize the Ti_3C_2 zinc-free anode. [124], [126]

4.5 Electrochemical Performance of Ti_3C_2 Zn-free anode

After analyzing the bulk electrolyte stability (HER), Zn deposition behavior, and surface SEI, the electrochemical performance is characterized by cycle life, coulombic efficiency, and rate capability.

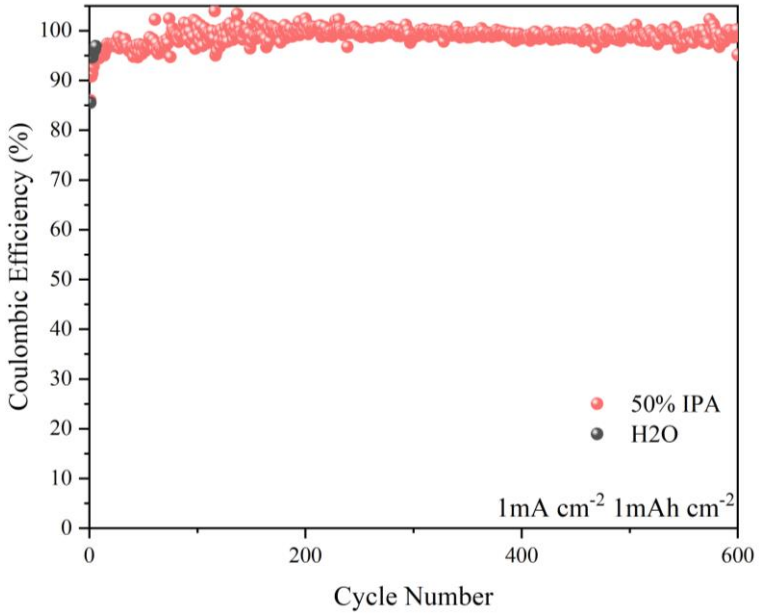

Figure 33 Coulombic efficiency and cycle life under different electrolyte systems

As shown in figure 33, coulombic efficiency and cycle life were tested using Ti_3C_2||Zn half-cells at a current density of 1mA cm^{-2} with a deposition capacity of 1mAh cm^{-2}. As illustrated in Figure 33, the cycle life in a pure H_2O electrolyte is limited to 14 hours, with rapid occurrence of short circuits. Additionally, the coulombic efficiency is only 92.25%. In contrast, the cycle life in the 50% IPA electrolyte is significantly improved, sustaining stable cycling for up to 1200 hours (600 cycles). Moreover, the average coulombic efficiency increases significantly to 98.95%. By introducing IPA as the co-solvent, the Zn plating/stripping coulombic efficiency increases by 6.7% and the cycle life extends by approximately 85 times.

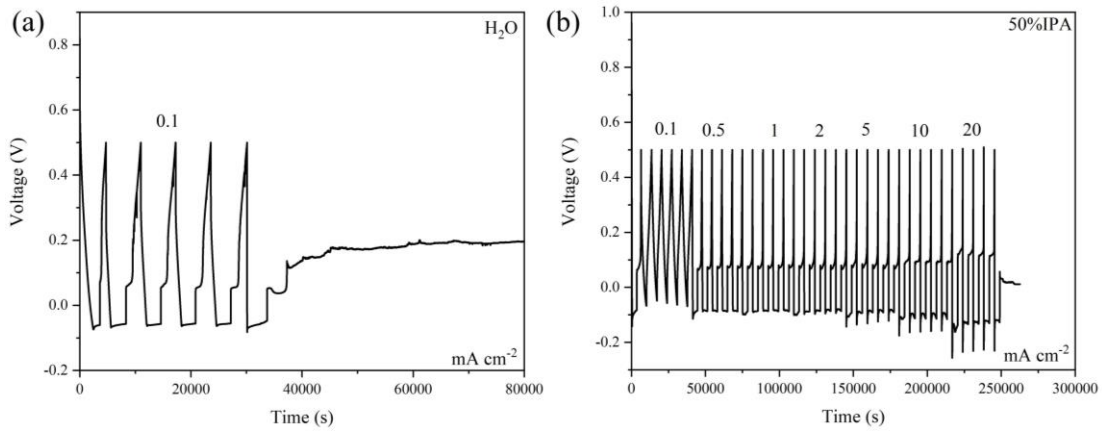

Figure 34 Rate performance of 50% IPA

In the rate test, half-cell in the pure water electrolyte quickly failed and could not be cycled, while in the 50% IPA electrolyte the half-cell could tolerate high current and high capacity of 20 mA cm^{-2} (20 mAh cm^{-2}) (figure 33).

	Pure H_2O	**50% IPA**	**Improvement**
Cycle life (h)	14	More than 1200	~ 85 times
ACE (%)	92.25	98.95	~6.7
Rate (mA cm^{-2})	-	20	-

Table 1 Comparison of Coulombic efficiency and cycle life of different electrolyte systems

On one hand, the introduction of IPA disrupts the original hydrogen bond network in water and forms a weak solvation structure, inhibiting the hydrogen evolution reaction. On the other hand, IPA facilitates directional zinc growth, leading to a larger nucleation overpotential, limiting 2D diffusion, aiding in SEI formation, and thus promoting more uniform zinc deposition. Consequently, the cycle life (~85 times), coulombic efficiency (~6.7%) and rate performance (20 mA cm^{-2} 20 mAh cm^{-2}) of the Ti_3C_2 zinc-free anode have been greatly improved. (form 1)

5 Discussion and Conclusion

5.1 PEG and IPA co-solvent improves the stability of Ti_3C_2 zinc-free anode

To answer the first research question in Section 1.5, the addition of PEG and IPA significantly enhances the stability of the Ti_3C_2 zinc-free anode.

PEG:

1. The cycle life was extended 42 times, increasing from 14 hours to 600 hours.
2. The coulombic efficiency improves by 6.7%, rising from 92.25% to 98.95%.
3. the Ti_3C_2 zinc-free anode achieves a higher rate performance of 10 mA cm^{-2} 10 mAh cm^{-2} with the addition of PEG.

IPA:

1. Specifically, the cycle life is extended nearly 85 times, increasing from 14 hours to 1200 hours.
2. The coulombic efficiency improves by 6.7%, rising from 92.25% to 98.95%.
3. Furthermore, the Ti_3C_2 zinc-free anode achieves a high rate performance of 20 mA cm^{-2} 20 mAh cm^{-2} with the addition of IPA.

Therefore, the incorporation of IPA substantially enhances various performance metrics of the Ti_3C_2 zinc-free anode.

5.2 The role of PEG and IPA in improving the zinc-free Ti_3C_2 anode

To answer the second research question, the role of PEG in enhancing the stability of the Ti_3C_2 zinc-free anode can be summarized as follows:

1. **Suppress hydrogen evolution:** The abundant strongly nucleophilic oxygen in PEG effectively disrupts the original hydrogen bond network in H_2O, thereby strengthening the OH covalent bond and inhibiting the occurrence of HER.
2. **Suppress 2D diffusion:** Adding PEG suppresses the 2D diffusion of adsorbed zinc particles, thus reducing dendrite growth.
3. **Oriented deposition**: PEG facilitates zinc growth along the (002) direction, further helping to suppress dendrite growth.

While PEG plays a significant role in mitigating hydrogen evolution and promoting uniform zinc deposition, its limited ionic conductivity constrains the cycling stability of the Ti_3C_2 anode to some extent.

Also, the role of IPA in enhancing the stability of the Ti_3C_2 zinc-free anode can be summarized as follows:

1. **Suppress hydrogen evolution**: With the addition of IPA, OTF^- anions compete with H_2O to enter the solvation sheath, effectively reducing the water content in the solvation sheath and thereby inhibiting the hydrogen evolution reaction (HER). Moreover, the oxygen functional groups in IPA,

which have strong nucleophilic ability, break the hydrogen bond network. This disruption strengthens the OH covalent bond, further limiting HER.

2. **Suppress 2D diffusion**: Furthermore, IPA inhibits the 2D diffusion of zinc on the existing zinc surface, which helps control the growth of the electrode's "effective surface area" and suppresses dendrite formation.

3. **Oriented deposition:** The addition of IPA can also help Zn grow parallel to the substrate along (002) direction, which may also lead to fewer dendrites.

4. **Formation of SEI Layer**: IPA contributes to the formation of a stable solid-electrolyte interphase (SEI) layer. This SEI layer helps in maintaining cycling stability, improving coulombic efficiency, and enhancing rate performance. The incorporation of OTF^- anions into the solvation sheath aids in the formation of this SEI layer.

In addition, it is worth noting that the formation of the weak solvation structure throughout the IPA part has two effects: (1) The introduction of OTF- anions into the solvation structure effectively reduces the content of H_2O, thereby inhibiting hydrogen evolution. (2) OTF- entering the solvation structure is more likely to react at the electrode interface to form a stable SEI, thereby enhancing the cycling stability of the electrode.

	HER current @-1.3V (mA)	Nucleation overpotential (mV)	Plateau Overpotential (mV)	CA Stable current (mA)	(002)/(001)	Average Coulombic Efficiency (%)	Cycle life (h)	Rate (mA cm^{-2})
H_2O	-0.47	75	51	-100	0.59	92.25	14	-
PEG	-0.05	91	82	-3	0.86	97.67	268	10
IPA	-0.08	100	62	-15	0.87	98.95	1200	20

Table 2 Comparison table of various performances of different electrolytes

A parallel comparison of IPA and PEG revealed that:

Orientational Growth: Both IPA and PEG similarly facilitate Zn growth in a specific orientation, as indicated by their comparable (002)/(101) ratios.
PEG for Suppression of HER and 2D Diffusion: PEG excels in suppressing HER and inhibiting 2D diffusion, indicating a stronger ability to prevent hydrogen evolution and limit grain growth. However, the poorer ionic conductivity of PEG electrolyte compared to IPA lead to more severe dendrite growth, limiting the overall cycle life of Ti_3C_2 anode in PEG electrolyte.
IPA for Nucleation Overpotential and SEI Formation: Compared with 50% PEG, Zn deposition in 50% IPA electrolyte exhibits a smaller plateau overpotential and a larger nucleation overpotential, which probably results in smaller grains (equation 11) at initial state. Furthermore, the addition of IPA can facilitate the formation of a SEI on the Ti_3C_2 surface. This SEI helps to guide the ion distribution, thereby promoting more uniform deposition processes.

5.3 The compromise between weak solvation and breaking hydrogen bond network

From 1.4.1 we know that there are two main ways to inhibit the hydrogen evolution reaction: reducing the H_2O content in the first solvation sheath and breaking the original hydrogen bond network in water.

Currently, there are two common strategies for reducing the H_2O content in the first solvation sheath:
1. **Adding solvents with high DN and high dielectric constant** to replace water in the solvation structure.
2. **Adding solvents with low DN and low dielectric constant** to weaken the dissolution of anions and cations in water, thereby reducing the contact between water and Zn ions.

These strategies have been well explained in Section 1.4.2 and will not be repeated here. However, the low DN required for weak solvation makes it more difficult to form hydrogen bonds with H_2O molecules, which in turn makes it harder to break the hydrogen bond network in water. As mentioned in Section 1.4.1, breaking the hydrogen bond network is crucial for inhibiting the hydrogen evolution reaction (HER) because it strengthens the OH covalent bond.

Therefore, this work did not use the traditional low DN weakly solvating solvent but instead used IPA solvent with a moderate DN (21) and extremely low dielectric constant (19.9, but still miscible with water) to attempt to break the hydrogen bond network and achieve weak solvation at the same time. This is confirmed in Chapters 3.1 and 3.2, where the hydrogen bond network is broken (figure 17), and the CIP ratio increases (figure 18). However, its inhibitory effect on HER is still limited, and the hydrogen evolution potential only shifts negatively by 24 mV (Figure 19 (c)). Therefore, more effective weak solvation or multi-component mixed solvents are still urgently needed for further development.

5.4 The importance of solvent conductivity

As summarized in Table 2, PEG outperforms IPA in terms of HER suppression and 2D diffusion inhibition. However, the cycle life of Ti_3C_2 anode in PEG electrolyte is less than half that of IPA.

Combining SEM and GCD analyses, we infer that the low ionic conductivity of PEG may induce a certain degree of concentration polarization and uneven concentration gradients on the surface of the Ti_3C_2 anode. This condition fosters the growth of dendrites which, as they extend, can potentially pierce the separator and cause a short circuit, thereby limiting the cycle life of anode in PEG electrolyte. Furthermore, poor ionic conductivity results in a higher overpotential, leading to increased energy loss.

In contrast, while IPA does not possess a better ability to inhibit hydrogen evolution and limit 2D diffusion compared to PEG, its higher ionic conductivity mitigates concentration polarization. Additionally, the formation of SEI also helps create a uniform ion concentration gradient to a certain extent, leading to an extended cycle life.

In summary, the cases of PEG and IPA provide valuable insights for the selection of co-solvents for zinc-free and zinc metal anodes. When screening co-solvents, it is crucial to consider not only conventional characterization but also the impact of ionic conductivity and overpotential on cycle stability.

6 Recommendations

1. **Understanding the molecular behavior of IPA and PEG on Ti_3C_2 surfaces**:

   Although we have demonstrated that the addition of IPA and PEG suppress the 2D diffusion, resulting in uniform deposition, the specific molecular behavior of IPA and PEG at the electrode interface remains unclear.

   Current research indicates that IPA has a more negative adsorption energy than water on certain MXene surfaces, such as Sc_2CO_2.[127] Additionally, studies have also confirmed that the characteristic adsorption of IPA at the zinc interface can lead to better zinc orientation.[112] Some studies have also pointed out that PEG can be adsorbed in parallel on the surface of Zn, thereby suppress 2D diffusion. [96]

   However, the specific molecular behavior of IPA and PEG on the Ti_3C_2 surface in this work may require further simulation calculations for clarity. For example, conducting molecular dynamics (MD) simulations focused on cosolvent interactions with the Ti_3C_2 surface would be beneficial. Specifically, calculating the difference in adsorption energy between cosolvent and water on the Ti_3C_2 surface would provide insights into their respective affinities. Additionally, density functional theory (DFT) calculations can offer valuable details on the atomic-scale behavior of cosolvent at the electrode interface. Furthermore, using rotating disk electrodes (RDE) is also a reasonable approach. By employing RDEs, we can exclude the influence of the concentration polarization (mass transport step) caused by higher electrolyte resistance and focus on the impact of the charge transfer step, which can provide additional insights into this issue.

2. **Ternary solution to further improve stability of Ti_3C_2 zinc-free anode**:

   While the 50% IPA electrolyte has significantly enhanced the performance of Ti_3C_2 zinc-free anodes compared to aqueous electrolytes, achieving higher and more stable coulombic efficiency remains crucial for specific applications.

   As shown in Figure 33, the coulombic efficiency of the 50% IPA group will continue to fluctuate within a range of 5%, which to some extent reflects the differences and instability between cycles. This instability between cycles may be due to the limited inhibitory effect of IPA on hydrogen evolution. Although it will not produce a large amount of hydrogen like in aqueous electrolytes, resulting in the battery exploding due to high internal pressure, the presence of tiny hydrogen bubbles adsorbed on the electrode surface could still impact surface behavior during charge and discharge cycles.[128]

   To address this, we propose introducing a solvent that enhances the inhibition of hydrogen evolution while maintaining weak solvation characteristics. For instance, diethyl carbonate (DEC), which is insoluble in water under standard conditions and possesses very low donor number (DN=16) and dielectric constant (ε=2.81)[129], could be considered. With the addition of OTF-, DEC can be mixed with IPA and water, thereby emphasizing the role of OTF- anions. In short, enhancing the inhibition of hydrogen evolution within the IPA-H_2O system represents a promising

strategy for developing ternary solvent systems that could propel the advancement of Ti_3C_2 zinc-free anodes.

Appendix

Extended Results

1. Corrosion test:

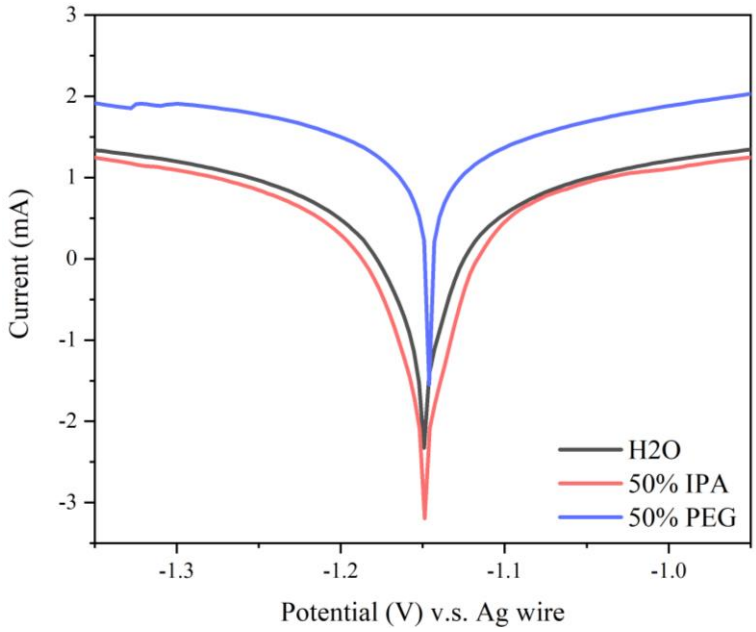

Extended figure 1 Tafel plots of bare zinc in different electrolytes

	H_2O	50% IPA	50% PEG
Corrosion Potential (V)	-1.149	-1.149	-1.146
Corrosion Current (mA)	3.653	3.170	32.223

Extended table 1 Corrosion potential and corrosion current of zinc in different electrolytes

Previously, the effects of different electrolytes on the HER and dendrites of Ti_3C_2 anode were analyzed in detail. While this study believes that corrosion is not the predominant factor (as shown by the absence of discernible corrosion products via XRD), it remains one among several challenges confronting zinc anodes. Therefore, Tafel test (extended figure 1 and extended table 1) is shown here as an extended result.

For 50% IPA and water electrolytes, the addition of IPA had minimal impact on the corrosion potential of zinc metal (-1.149 mV). Additionally, the corrosion current showed a slight decrease with the addition of IPA (from 3.653 mA in water to 3.170 mA in 50% IPA). This lower corrosion current density corresponds to a weaker corrosion reaction.

In contrast, for 50% PEG and water electrolytes, the addition of PEG resulted in a higher corrosion potential (-1.149 mV in water, -1.146 mV in 50% PEG). However, the addition of PEG caused a significantly larger corrosion current density (3.653 mA in water, 32.223 mA in 50% PEG). Although a

higher corrosion potential indicates that corrosion reactions are more difficult to initiate, the excessively high corrosion current suggests that, when corrosion occurs, it may be more severe for the metal.

2. Zn||Zn Symmetric cell

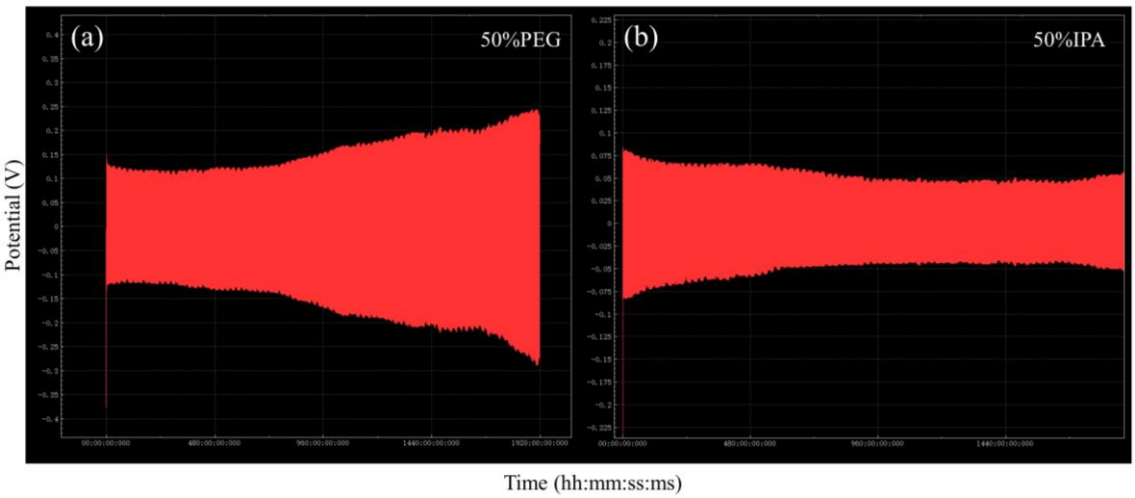

Extended figure 2 Plating/stripping cycling stability of Zn symmetric cells. Long-term galvanostatic cycling performance of symmetrical cells in (a) the 50%PEG and (b) 50% IPA electrolytes at 1 mA cm^{-2} and an areal capacity of 1 mA h cm^{-2}

To verify the adaptability of 50% PEG and 50% IPA to zinc metal anodes, Zn||Zn symmetric cells were tested. It was observed that the cycle life of the symmetric cells in both 50% PEG and 50% IPA electrolytes lasted for more than 1900 hours and continued to cycle. In comparison, the cycle life of symmetric cells in H_2O electrolyte, as reported in other literature, often struggles to exceed 500 hours. [86] This demonstrates the suitability of 50% PEG and 50% IPA for zinc anodes.

Additionally, the overpotential of the symmetric cell in the 50% PEG electrolyte gradually increased, likely due to poor ionic conductivity and the accumulation of "dead zinc." In contrast, the overpotential of the symmetric cell in the 50% IPA electrolyte initially decreased and then stabilized, highlighting the superiority of 50% IPA in extending the cycle life.

3. IPA-PEG-H_2O Ternary solvent electrolyte

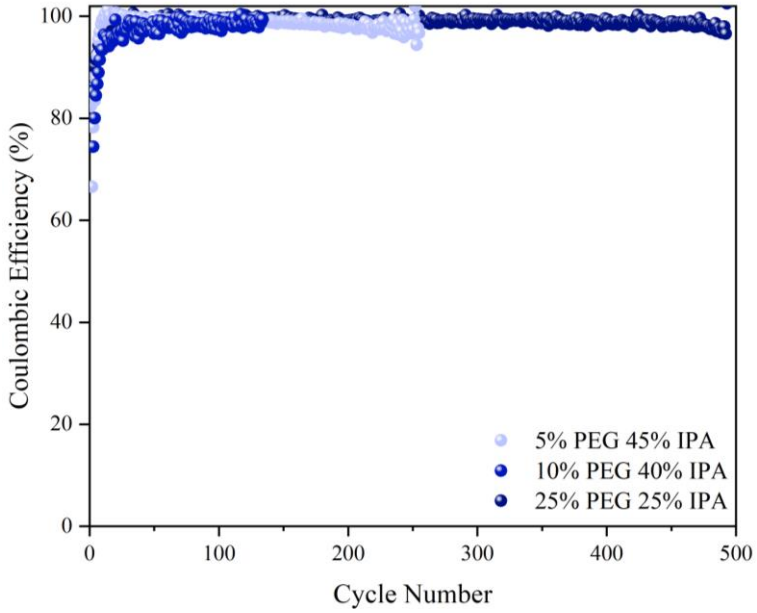

Extended figure 3 Coulombic efficiency and cycle life of Ti_3C_2 in IPA-PEG-H_2O electrolytes with different solvent ratio.

Since IPA and PEG play different roles in the cycle stability of the Ti_3C_2 anode, we developed an IPA-PEG-H_2O ternary solvent electrolyte to attempt to further improve the cycle stability of Ti_3C_2.

As shown in the figure, the Ti_3C_2 anode exhibits a shorter cycle life in IPA-PEG-H_2O ternary solvent electrolytes at different concentrations compared to 50% IPA (more than 1200h). Specifically, in the electrolytes containing 5% PEG 45% IPA(~500h) and 10% PEG 40% IPA (~125h), the Ti_3C_2 anode shows a lower cycle life than in 50% PEG. This indicates that the IPA-PEG-H_2O ternary solvent electrolyte does not improve the cycle stability of the Ti_3C_2 anode.

Based on previous tests, we propose two hypotheses. First, the addition of PEG may affect the intrinsic ionic conductivity of IPA electrolyte, leading to more severe dendrite formation and a shorter cycle life. However, this hypothesis does not explain why the mixed electrolyte performs worse than the 50% PEG electrolyte alone. Second, the distinct molecular behaviors of PEG and IPA on the Ti_3C_2 surface may cause conflicts. For instance, IPA, due to its weak solvating ability, may facilitate the incorporation of OTF- anions into the solvated structure to form a SEI layer, while PEG, which tends to adsorb parallel to the zinc surface, may hinder the formation of a stable SEI. [96] These conflicting molecular interactions could potentially reduce the cycle life of the Ti_3C_2 anode. Further calculations and characterizations are needed to confirm this hypothesis.

Reference

[1] B. Obama, “The irreversible momentum of clean energy,” *Science*, vol. 355, no. 6321, pp. 126–129, Jan. 2017, doi: 10.1126/science.aam6284.

[2] Y. Han *et al.*, “Interface issues of lithium metal anode for high-energy batteries: Challenges, strategies, and perspectives”.

[3] A. Innocenti, “A critical discussion of the current availability of lithium and zinc for use in batteries,” *Nat. Commun.*, 2024.

[4] L. Tang, “Zn-based batteries for sustainable energy storage: strategies and mechanisms,” *Chem Soc Rev*, 2024.

[5] S. Zhao *et al.*, “Unravelling the reaction chemistry and degradation mechanism in aqueous Zn/MnO_2 rechargeable batteries,” *J. Mater. Chem. A*, vol. 6, no. 14, pp. 5733–5739, 2018, doi: 10.1039/C8TA01031E.

[6] Z. Li, S. Ganapathy, Y. Xu, Z. Zhou, M. Sarilar, and M. Wagemaker, “Mechanistic Insight into the Electrochemical Performance of Zn/VO_2 Batteries with an Aqueous $ZnSO_4$ Electrolyte,” *Adv. Energy Mater.*, vol. 9, no. 22, p. 1900237, Jun. 2019, doi: 10.1002/aenm.201900237.

[7] Y. Li *et al.*, “Prussian blue analogs cathodes for aqueous zinc ion batteries,” *Mater. Today Energy*, vol. 29, p. 101095, Oct. 2022, doi: 10.1016/j.mtener.2022.101095.

[8] P. Liang *et al.*, “Highly Reversible Zn Anode Enabled by Controllable Formation of Nucleation Sites for Zn-Based Batteries,” *Adv. Funct. Mater.*, vol. 30, no. 13, p. 1908528, Mar. 2020, doi: 10.1002/adfm.201908528.

[9] D. Wang *et al.*, “Insight on Organic Molecules in Aqueous Zn-Ion Batteries with an Emphasis on the Zn Anode Regulation,” *Adv. Energy Mater.*, vol. 12, no. 9, p. 2102707, Mar. 2022, doi: 10.1002/aenm.202102707.

[10] A. Pei, G. Zheng, F. Shi, Y. Li, and Y. Cui, “Nanoscale Nucleation and Growth of Electrodeposited Lithium Metal,” *Nano Lett.*, vol. 17, no. 2, pp. 1132–1139, Feb. 2017, doi: 10.1021/acs.nanolett.6b04755.

[11] Z. Li, Y. Zhou, Y. Wang, and Y. Lu, “Solvent-Mediated Li_2S Electrodeposition: A Critical Manipulator in Lithium–Sulfur Batteries,” *Adv. Energy Mater.*, vol. 9, no. 1, p. 1802207, Jan. 2019, doi: 10.1002/aenm.201802207.

[12] E. R. Cooper, M. Li, I. Gentle, Q. Xia, and R. Knibbe, “A Deeper Understanding of Metal Nucleation and Growth in Rechargeable Metal Batteries Through Theory and Experiment,” *Angew. Chem. Int. Ed.*, vol. 62, no. 51, p. e202309247, Dec. 2023, doi: 10.1002/anie.202309247.

[13] Q. Li *et al.*, “Homogeneous Interface Conductivity for Lithium Dendrite-Free Anode,” *ACS Energy Lett.*, vol. 3, no. 9, pp. 2259–2266, Sep. 2018, doi: 10.1021/acsenergylett.8b01244.

[14] K. Liu, Y. Liu, D. Lin, A. Pei, and Y. Cui, “Materials for lithium-ion battery safety,” *Sci. Adv.*, 2018.

[15] Z. Li and A. W. Robertson, “Electrolyte engineering strategies for regulation of the Zn metal anode in aqueous Zn-ion batteries,” *Battery Energy*, vol. 2, no. 1, p. 20220029, Jan. 2023, doi: 10.1002/bte2.20220029.

[16] A. Bewick, M. Fleischmann, and H. R. Thirsk, “Kinetics of the electrocrystallization of thin films of calomel,” *Trans. Faraday Soc.*, vol. 58, p. 2200, 1962, doi: 10.1039/tf9625802200.

[17] B. R. Scharifker and J. Mostany, “NUCLEATION WITH DIFFUSION CONTROLLED”.

[18] I. Danaee, “2D–3D nucleation and growth of palladium on graphite electrode,” *J. Ind. Eng. Chem.*, vol. 19, no. 3, pp. 1008–1013, May 2013, doi: 10.1016/j.jiec.2012.11.024.

[19] A. Bayaguud, X. Luo, Y. Fu, and C. Zhu, “Cationic Surfactant-Type Electrolyte Additive Enables Three-Dimensional Dendrite-Free Zinc Anode for Stable Zinc-Ion Batteries,” *ACS Energy Lett.*, vol. 5, no. 9, pp. 3012–3020, Sep. 2020, doi: 10.1021/acsenergylett.0c01792.

[20] K. Zhu *et al.*, “Engineering an electrostatic field layer for high-rate and dendrite-free Zn metal anodes,” *Energy Environ. Sci.*, vol. 16, no. 8, pp. 3612–3622, 2023, doi: 10.1039/D3EE01724A.

[21] W. Zhang, H. L. Zhuang, L. Fan, L. Gao, and Y. Lu, “A ‘cation-anion regulation’ synergistic anode host for dendrite-free lithium metal batteries,” *Sci. Adv.*, vol. 4, no. 2, p. eaar4410, Feb. 2018, doi: 10.1126/sciadv.aar4410.

[22] Q. Yang *et al.*, “Do Zinc Dendrites Exist in Neutral Zinc Batteries: A Developed Electrohealing Strategy to In Situ Rescue In-Service Batteries,” *Adv. Mater.*, vol. 31, no. 43, p. 1903778, Oct. 2019, doi: 10.1002/adma.201903778.
[23] C. Zhu, P. Li, G. Xu, H. Cheng, and G. Gao, “Recent progress and challenges of Zn anode modification materials in aqueous Zn-ion batteries,” *Coord. Chem. Rev.*, vol. 485, p. 215142, Jun. 2023, doi: 10.1016/j.ccr.2023.215142.
[24] H. J. S. Sand, “III. *On the concentration at the electrodes in a solution, with special reference to the liberation of hydrogen by electrolysis of a mixture of copper sulphate and sulphuric acid*,” *Lond. Edinb. Dublin Philos. Mag. J. Sci.*, vol. 1, no. 1, pp. 45–79, Jan. 1901, doi: 10.1080/14786440109462590.
[25] P. Bai, J. Li, F. R. Brushett, and M. Z. Bazant, “Transition of lithium growth mechanisms in liquid electrolytes,” *Energy Environ. Sci.*, vol. 9, no. 10, pp. 3221–3229, 2016, doi: 10.1039/C6EE01674J.
[26] M. A. Ibrahim, “Improving the throwing power of acidic zinc sulfate electroplating baths,” *J. Chem. Technol. Biotechnol.*, vol. 75, no. 8, pp. 745–755, Aug. 2000, doi: 10.1002/1097-4660(200008)75:8<745::AID-JCTB274>3.0.CO;2-5.
[27] Z. Yi, G. Chen, F. Hou, L. Wang, and J. Liang, “Strategies for the Stabilization of Zn Metal Anodes for Zn-Ion Batteries,” *Adv. Energy Mater.*, vol. 11, no. 1, p. 2003065, Jan. 2021, doi: 10.1002/aenm.202003065.
[28] C. Li, X. Xie, S. Liang, and J. Zhou, “Issues and Future Perspective on Zinc Metal Anode for Rechargeable Aqueous Zinc-ion Batteries,” *ENERGY Environ. Mater.*, vol. 3, no. 2, pp. 146–159, Jun. 2020, doi: 10.1002/eem2.12067.
[29] A. Bayaguud, Y. Fu, and C. Zhu, “Interfacial parasitic reactions of zinc anodes in zinc ion batteries: Underestimated corrosion and hydrogen evolution reactions and their suppression strategies,” *J. Energy Chem.*, vol. 64, pp. 246–262, Jan. 2022, doi: 10.1016/j.jechem.2021.04.016.
[30] Z. Cai *et al.*, “Chemically resistant Cu–Zn/Zn composite anode for long cycling aqueous batteries,” *Energy Storage Mater.*, vol. 27, pp. 205–211, May 2020, doi: 10.1016/j.ensm.2020.01.032.
[31] J. H. Jo *et al.*, “New Insight on Open-Structured Sodium Vanadium Oxide as High-Capacity and Long Life Cathode for Zn–Ion Storage: Structure, Electrochemistry, and First-Principles Calculation,” *Adv. Energy Mater.*, vol. 10, no. 40, p. 2001595, Oct. 2020, doi: 10.1002/aenm.202001595.
[32] G. Yang, Q. Li, K. Ma, C. Hong, and C. Wang, “The degradation mechanism of vanadium oxide-based aqueous zinc-ion batteries,” *J. Mater. Chem. A*, vol. 8, no. 16, pp. 8084–8095, 2020, doi: 10.1039/D0TA00615G.
[33] Y. Liang, M. Qiu, P. Sun, and W. Mai, “Comprehensive Review of Electrolyte Modification Strategies for Stabilizing Zn Metal Anodes,” *Adv. Funct. Mater.*, vol. 33, no. 51, p. 2304878, Dec. 2023, doi: 10.1002/adfm.202304878.
[34] C. Li *et al.*, “Roadmap on the protective strategies of zinc anodes in aqueous electrolyte,” *Energy Storage Mater.*, vol. 44, pp. 104–135, Jan. 2022, doi: 10.1016/j.ensm.2021.10.020.
[35] S. Xie, Y. Li, and L. Dong, “Stable anode-free zinc-ion batteries enabled by alloy network-modulated zinc deposition interface,” *J. Energy Chem.*, vol. 76, pp. 32–40, Jan. 2023, doi: 10.1016/j.jechem.2022.08.040.
[36] Y. Zhu, Y. Cui, and H. N. Alshareef, “An Anode-Free Zn–MnO_2 Battery,” *Nano Lett.*, vol. 21, no. 3, pp. 1446–1453, Feb. 2021, doi: 10.1021/acs.nanolett.0c04519.
[37] M. Cui *et al.*, “Quasi-Isolated Au Particles as Heterogeneous Seeds To Guide Uniform Zn Deposition for Aqueous Zinc-Ion Batteries,” *ACS Appl. Energy Mater.*, vol. 2, no. 9, pp. 6490–6496, Sep. 2019, doi: 10.1021/acsaem.9b01063.
[38] Y. Zhang, J. D. Howe, S. Ben-Yoseph, Y. Wu, and N. Liu, “Unveiling the Origin of Alloy-Seeded and Nondendritic Growth of Zn for Rechargeable Aqueous Zn Batteries,” *ACS Energy Lett.*, vol. 6, no. 2, pp. 404–412, Feb. 2021, doi: 10.1021/acsenergylett.0c02343.
[39] H. Li, W. Jia, P. Chen, L. Wang, X. Yan, and Y.-Y. Yang, “Zinc deposition characteristics on different substrates for aqueous zinc ion battery,” *Appl. Surf. Sci.*, vol. 607, p. 155111, Jan. 2023, doi: 10.1016/j.apsusc.2022.155111.

[40] Y. Yin *et al.*, “Dendrite-Free Zinc Deposition Induced by Tin-Modified Multifunctional 3D Host for Stable Zinc-Based Flow Battery,” *Adv. Mater.*, vol. 32, no. 6, p. 1906803, Feb. 2020, doi: 10.1002/adma.201906803.
[41] K. Xu *et al.*, “A three-dimensional zincophilic nano-copper host enables dendrite-free and anode-free Zn batteries,” *Mater. Today Energy*, vol. 34, p. 101284, Jun. 2023, doi: 10.1016/j.mtener.2023.101284.
[42] X. Zheng *et al.*, “Constructing robust heterostructured interface for anode-free zinc batteries with ultrahigh capacities,” *Nat. Commun.*, vol. 14, no. 1, p. 76, Jan. 2023, doi: 10.1038/s41467-022-35630-6.
[43] H. Chen *et al.*, “Flexible $Ti_3C_2T_x$ /Nanocellulose Hybrid Film as a Stable Zn-free Anode for Aqueous Hybrid Zn–Li Batteries,” *ACS Appl. Mater. Interfaces*, vol. 14, no. 5, pp. 6876–6884, Feb. 2022, doi: 10.1021/acsami.1c23402.
[44] X. Li *et al.*, “Toward a Practical Zn Powder Anode: $Ti_3C_2T_x$ MXene as a Lattice-Match Electrons/Ions Redistributor,” *ACS Nano*, vol. 15, no. 9, pp. 14631–14642, Sep. 2021, doi: 10.1021/acsnano.1c04354.
[45] F. Ming *et al.*, “Co-Solvent Electrolyte Engineering for Stable Anode-Free Zinc Metal Batteries,” *J. Am. Chem. Soc.*, vol. 144, no. 16, pp. 7160–7170, Apr. 2022, doi: 10.1021/jacs.1c12764.
[46] M. Naguib *et al.*, “Two-Dimensional Nanocrystals Produced by Exfoliation of Ti_3AlC_2,” *Adv. Mater.*, vol. 23, no. 37, pp. 4248–4253, Oct. 2011, doi: 10.1002/adma.201102306.
[47] T. S. Mathis *et al.*, “Modified MAX Phase Synthesis for Environmentally Stable and Highly Conductive Ti_3C_2 MXene,” *ACS Nano*, vol. 15, no. 4, pp. 6420–6429, Apr. 2021, doi: 10.1021/acsnano.0c08357.
[48] A. Lipatov *et al.*, “Elastic properties of 2D Ti3C2Tx MXene monolayers and bilayers,” *Sci. Adv.*, 2018.
[49] Y. Gogotsi and Q. Huang, “MXenes: Two-Dimensional Building Blocks for Future Materials and Devices,” *ACS Nano*, vol. 15, no. 4, pp. 5775–5780, Apr. 2021, doi: 10.1021/acsnano.1c03161.
[50] M. Naguib *et al.*, “Two-Dimensional Transition Metal Carbides,” *ACS Nano*, vol. 6, no. 2, pp. 1322–1331, Feb. 2012, doi: 10.1021/nn204153h.
[51] M. Naguib *et al.*, “New Two-Dimensional Niobium and Vanadium Carbides as Promising Materials for Li-Ion Batteries,” *J. Am. Chem. Soc.*, vol. 135, no. 43, pp. 15966–15969, Oct. 2013, doi: 10.1021/ja405735d.
[52] K. Maleski, V. N. Mochalin, and Y. Gogotsi, “Dispersions of Two-Dimensional Titanium Carbide MXene in Organic Solvents,” *Chem. Mater.*, vol. 29, no. 4, pp. 1632–1640, Feb. 2017, doi: 10.1021/acs.chemmater.6b04830.
[53] P. Urbankowski *et al.*, “Synthesis of two-dimensional titanium nitride Ti_4N_3 (MXene),” *Nanoscale*, vol. 8, no. 22, pp. 11385–11391, 2016, doi: 10.1039/C6NR02253G.
[54] M. Han *et al.*, “Beyond $Ti_3C_2T_x$: MXenes for Electromagnetic Interference Shielding,” *ACS Nano*, vol. 14, no. 4, pp. 5008–5016, Apr. 2020, doi: 10.1021/acsnano.0c01312.
[55] I. Persson *et al.*, “Tailoring Structure, Composition, and Energy Storage Properties of MXenes from Selective Etching of In-Plane, Chemically Ordered MAX Phases,” *Small*, vol. 14, no. 17, p. 1703676, Apr. 2018, doi: 10.1002/smll.201703676.
[56] B. Anasori *et al.*, “Two-Dimensional, Ordered, Double Transition Metals Carbides (MXenes),” *ACS Nano*, vol. 9, no. 10, pp. 9507–9516, Oct. 2015, doi: 10.1021/acsnano.5b03591.
[57] S. K. Nemani *et al.*, “High-Entropy 2D Carbide MXenes: $TiVNbMoC_3$ and $TiVCrMoC_3$,” *ACS Nano*, vol. 15, no. 8, pp. 12815–12825, Aug. 2021, doi: 10.1021/acsnano.1c02775.
[58] Z. Du *et al.*, “High-Entropy Carbonitride MAX Phases and Their Derivative MXenes,” *Adv. Energy Mater.*, vol. 12, no. 6, p. 2103228, Feb. 2022, doi: 10.1002/aenm.202103228.
[59] C. E. Park, R. A. Senthil, G. H. Jeong, and M. Y. Choi, “Architecting the High-Entropy Oxides on 2D MXene Nanosheets by Rapid Microwave-Heating Strategy with Robust Photoelectrochemical Oxygen Evolution Performance,” *Small*, vol. 19, no. 27, p. 2207820, Jul. 2023, doi: 10.1002/smll.202207820.
[60] Q. Liang *et al.*, “High-Entropy MXene as Bifunctional Mediator toward Advanced Li–S Full Batteries,” *ACS Nano*, vol. 18, no. 3, pp. 2395–2408, Jan. 2024, doi: 10.1021/acsnano.3c10731.

[61] A. VahidMohammadi, J. Rosen, and Y. Gogotsi, “The world of two-dimensional carbides and nitrides (MXenes),” *Science*, vol. 372, no. 6547, p. eabf1581, Jun. 2021, doi: 10.1126/science.abf1581.
[62] Y. Li *et al.*, “A general Lewis acidic etching route for preparing MXenes with enhanced electrochemical performance in non-aqueous electrolyte,” *Nat. Mater.*, vol. 19, no. 8, pp. 894–899, Aug. 2020, doi: 10.1038/s41563-020-0657-0.
[63] D. Wang *et al.*, “Direct synthesis and chemical vapor deposition of 2D carbide and nitride MXenes,” *Science*, vol. 379, no. 6638, pp. 1242–1247, Mar. 2023, doi: 10.1126/science.add9204.
[64] O. Mashtalir *et al.*, “Intercalation and delamination of layered carbides and carbonitrides,” *Nat. Commun.*, vol. 4, no. 1, p. 1716, Apr. 2013, doi: 10.1038/ncomms2664.
[65] Q. Tang, Z. Zhou, and P. Shen, “Are MXenes Promising Anode Materials for Li Ion Batteries? Computational Studies on Electronic Properties and Li Storage Capability of Ti_3C_2 and $Ti_3C_2X_2$ (X = F, OH) Monolayer,” *J. Am. Chem. Soc.*, vol. 134, no. 40, pp. 16909–16916, Oct. 2012, doi: 10.1021/ja308463r.
[66] Y. Liu, H. Xiao, and W. A. Goddard, “Schottky-Barrier-Free Contacts with Two-Dimensional Semiconductors by Surface-Engineered MXenes,” *J. Am. Chem. Soc.*, vol. 138, no. 49, pp. 15853–15856, Dec. 2016, doi: 10.1021/jacs.6b10834.
[67] S. Lai *et al.*, “Surface group modification and carrier transport properties of layered transition metal carbides (Ti_2CT_x, T: –OH, –F and –O),” *Nanoscale*, vol. 7, no. 46, pp. 19390–19396, 2015, doi: 10.1039/C5NR06513E.
[68] M. Ghidiu, M. R. Lukatskaya, M.-Q. Zhao, Y. Gogotsi, and M. W. Barsoum, “Conductive two-dimensional titanium carbide ‘clay’ with high volumetric capacitance,” *Nature*, vol. 516, no. 7529, pp. 78–81, Dec. 2014, doi: 10.1038/nature13970.
[69] Y.-J. Kim *et al.*, “Etching Mechanism of Monoatomic Aluminum Layers during MXene Synthesis,” *Chem. Mater.*, vol. 33, no. 16, pp. 6346–6355, Aug. 2021, doi: 10.1021/acs.chemmater.1c01263.
[70] M. A. Hope *et al.*, “NMR reveals the surface functionalisation of Ti_3C_2 MXene,” *Phys. Chem. Chem. Phys.*, vol. 18, no. 7, pp. 5099–5102, 2016, doi: 10.1039/C6CP00330C.
[71] H. Tang *et al.*, “In Situ Formed Protective Barrier Enabled by Sulfur@Titanium Carbide (MXene) Ink for Achieving High-Capacity, Long Lifetime Li-S Batteries,” *Adv. Sci.*, vol. 5, no. 9, p. 1800502, Sep. 2018, doi: 10.1002/advs.201800502.
[72] S.-Y. Pang *et al.*, “Universal Strategy for HF-Free Facile and Rapid Synthesis of Two-dimensional MXenes as Multifunctional Energy Materials,” *J. Am. Chem. Soc.*, vol. 141, no. 24, pp. 9610–9616, Jun. 2019, doi: 10.1021/jacs.9b02578.
[73] M. Peng, M. Dong, W. Wei, H. Xu, C. Liu, and C. Shen, “The introduction of amino termination on Ti3C2 MXene surface for its flexible film with excellent property,” *Carbon*, vol. 179, pp. 400–407, Jul. 2021, doi: 10.1016/j.carbon.2021.04.049.
[74] M. Peng, Z. Wu, W. Wei, H. Xu, C. Liu, and C. Shen, “Amino Termination of Ti_3C_2 MXene Induces its Graphene Hybridized Film with Enhanced Ordered Nanostructure and Excellent Multiperformance,” *Adv. Mater. Interfaces*, vol. 9, no. 18, p. 2102418, Jun. 2022, doi: 10.1002/admi.202102418.
[75] C. Zhou *et al.*, “Hybrid organic–inorganic two-dimensional metal carbide MXenes with amido- and imido-terminated surfaces,” *Nat. Chem.*, vol. 15, no. 12, pp. 1722–1729, Dec. 2023, doi: 10.1038/s41557-023-01288-w.
[76] X. Zhao *et al.*, “Electrocatalytic enhancement mechanism of cobalt single atoms anchored on different MXene substrates in oxygen and hydrogen evolution reactions,” *EcoMat*, vol. 5, no. 2, p. e12293, Feb. 2023, doi: 10.1002/eom2.12293.
[77] C. Xu *et al.*, “Large-area high-quality 2D ultrathin Mo2C superconducting crystals,” *Nat. Mater.*, vol. 14, no. 11, pp. 1135–1141, Nov. 2015, doi: 10.1038/nmat4374.
[78] J. Vacík *et al.*, “Ion sputtering for preparation of thin MAX and MXene phases,” *Radiat. Eff. Defects Solids*, vol. 175, no. 1–2, pp. 177–189, Jan. 2020, doi: 10.1080/10420150.2020.1718142.
[79] Z. Sun *et al.*, “Generalized self-assembly of scalable two-dimensional transition metal oxide nanosheets,” *Nat. Commun.*, vol. 5, no. 1, p. 3813, May 2014, doi: 10.1038/ncomms4813.

[80] D. Dong, J. Xie, Z. Liang, and Y.-C. Lu, “Tuning Intermolecular Interactions of Molecular Crowding Electrolyte for High-Performance Aqueous Batteries,” *ACS Energy Lett.*, vol. 7, no. 1, pp. 123–130, Jan. 2022, doi: 10.1021/acsenergylett.1c02064.
[81] Y. Kang *et al.*, “Modulating the Electrolyte Inner Solvation Structure via Low Polarity Co-solvent for Low-Temperature Aqueous Zinc-Ion Batteries,” *ENERGY Environ. Mater.*, p. e12707, Jan. 2024, doi: 10.1002/eem2.12707.
[82] Z. Li *et al.*, “A co-solvent in aqueous electrolyte towards ultralong-life rechargeable zinc-ion batteries,” *Energy Storage Mater.*, vol. 56, pp. 174–182, Feb. 2023, doi: 10.1016/j.ensm.2023.01.020.
[83] H. Yu *et al.*, “Insight on the Double-Edged Sword Role of Water Molecules in the Anode of Aqueous Zinc-Ion Batteries,” *Small Struct.*, vol. 3, no. 12, p. 2200143, Dec. 2022, doi: 10.1002/sstr.202200143.
[84] F. Wang *et al.*, “Highly reversible zinc metal anode for aqueous batteries,” *Nat. Mater.*, vol. 17, no. 6, pp. 543–549, Jun. 2018, doi: 10.1038/s41563-018-0063-z.
[85] F. Yang *et al.*, “Understanding H_2 Evolution Electrochemistry to Minimize Solvated Water Impact on Zinc-Anode Performance,” *Adv. Mater.*, vol. 34, no. 45, p. 2206754, Nov. 2022, doi: 10.1002/adma.202206754.
[86] L. Cao *et al.*, “Solvation Structure Design for Aqueous Zn Metal Batteries,” *J. Am. Chem. Soc.*, vol. 142, no. 51, pp. 21404–21409, Dec. 2020, doi: 10.1021/jacs.0c09794.
[87] G. Ma *et al.*, “Reshaping the electrolyte structure and interface chemistry for stable aqueous zinc batteries,” *Energy Storage Mater.*, vol. 47, pp. 203–210, May 2022, doi: 10.1016/j.ensm.2022.02.019.
[88] B. Raza *et al.*, “Zn anode sustaining high rate and high loading in organic electrolyte for rechargeable batteries,” *Energy Storage Mater.*, vol. 46, pp. 523–534, Apr. 2022, doi: 10.1016/j.ensm.2022.01.043.
[89] W. Deng, Z. Xu, and X. Wang, “High-donor electrolyte additive enabling stable aqueous zinc-ion batteries,” *Energy Storage Mater.*, vol. 52, pp. 52–60, Nov. 2022, doi: 10.1016/j.ensm.2022.07.032.
[90] F. Wu *et al.*, “Achieving Highly Reversible Zinc Anodes via N, N-Dimethylacetamide Enabled Zn-Ion Solvation Regulation,” *Small*, vol. 18, no. 27, p. 2202363, Jul. 2022, doi: 10.1002/smll.202202363.
[91] X. Shi, J. Xie, J. Wang, S. Xie, Z. Yang, and X. Lu, “A weakly solvating electrolyte towards practical rechargeable aqueous zinc-ion batteries,” *Nat. Commun.*, vol. 15, no. 1, p. 302, Jan. 2024, doi: 10.1038/s41467-023-44615-y.
[92] X. Cao *et al.*, “Weak Solvation Effect Induced Optimal Interfacial Chemistry Enables Highly Durable Zn Anodes for Aqueous Zn-Ion Batteries,” *Angew. Chem. Int. Ed.*, vol. 63, no. 6, p. e202317302, Feb. 2024, doi: 10.1002/anie.202317302.
[93] Y. Yang *et al.*, “Weakly Solvating Effect Spawning Reliable Interfacial Chemistry for Aqueous Zn/Na Hybrid Batteries,” *Adv. Energy Mater.*, vol. 13, no. 12, p. 2203729, Mar. 2023, doi: 10.1002/aenm.202203729.
[94] L. Miao *et al.*, “Aqueous Electrolytes with Hydrophobic Organic Cosolvents for Stabilizing Zinc Metal Anodes,” *ACS Nano*, vol. 16, no. 6, pp. 9667–9678, Jun. 2022, doi: 10.1021/acsnano.2c02996.
[95] Y. Jin *et al.*, “Stabilizing Zinc Anode Reactions by Polyethylene Oxide Polymer in Mild Aqueous Electrolytes,” *Adv. Funct. Mater.*, vol. 30, no. 43, p. 2003932, Oct. 2020, doi: 10.1002/adfm.202003932.
[96] Y. Wu *et al.*, “Electrolyte engineering enables stable Zn-Ion deposition for long-cycling life aqueous Zn-ion batteries,” *Energy Storage Mater.*, vol. 45, pp. 1084–1091, Mar. 2022, doi: 10.1016/j.ensm.2021.11.003.
[97] C. Berthomieu and R. Hienerwadel, “Fourier transform infrared (FTIR) spectroscopy,” *Photosynth. Res.*, vol. 101, no. 2–3, pp. 157–170, Sep. 2009, doi: 10.1007/s11120-009-9439-x.
[98] J. Epp, “X-ray diffraction (XRD) techniques for materials characterization,” in *Materials Characterization Using Nondestructive Evaluation (NDE) Methods*, Elsevier, 2016, pp. 81–124. doi: 10.1016/B978-0-08-100040-3.00004-3.

[99] W. Zhou, R. P. Apkarian, Z. L. Wang, and D. Joy, “Fundamentals of Scanning Electron Microscopy”.
[100] A. M. Venezia, “X-ray photoelectron spectroscopy (XPS) for catalysts characterization,” *Catal. Today*, vol. 77, no. 4, pp. 359–370, Jan. 2003, doi: 10.1016/S0920-5861(02)00380-2.
[101] M. Aziz and A. F. Ismail, “X-Ray Photoelectron Spectroscopy (XPS),” in *Membrane Characterization*, Elsevier, 2017, pp. 81–93. doi: 10.1016/B978-0-444-63776-5.00005-X.
[102] A. Ch. Lazanas and M. I. Prodromidis, “Electrochemical Impedance Spectroscopy─A Tutorial,” *ACS Meas. Sci. Au*, vol. 3, no. 3, pp. 162–193, Jun. 2023, doi: 10.1021/acsmeasuresciau.2c00070.
[103] J. E. B. Randles, “Kinetics of rapid electrode reactions,” *Discuss. Faraday Soc.*, vol. 1, p. 11, 1947, doi: 10.1039/df9470100011.
[104] R. S. Nicholson and Irving. Shain, “Theory of Stationary Electrode Polarography. Single Scan and Cyclic Methods Applied to Reversible, Irreversible, and Kinetic Systems.,” *Anal. Chem.*, vol. 36, no. 4, pp. 706–723, Apr. 1964, doi: 10.1021/ac60210a007.
[105] G. Trejo, H. Ruiz, R. O. Borges, and Y. Meas, “In¯uence of polyethoxylated additives on zinc electrodeposition from acidic solutions”.
[106] Z. Cao *et al.*, “Ultrastable Zinc Anode by Simultaneously Manipulating Solvation Sheath and Inducing Oriented Deposition with PEG Stability Promoter,” *Small*, vol. 18, no. 6, p. 2103345, Feb. 2022, doi: 10.1002/smll.202103345.
[107] Q. Zhang *et al.*, “Modulating electrolyte structure for ultralow temperature aqueous zinc batteries,” *Nat. Commun.*, vol. 11, no. 1, p. 4463, Sep. 2020, doi: 10.1038/s41467-020-18284-0.
[108] J.-B. Brubach *et al.*, “Dependence of Water Dynamics upon Confinement Size,” *J. Phys. Chem. B*, vol. 105, no. 2, pp. 430–435, Jan. 2001, doi: 10.1021/jp002983s.
[109] Y. Ding *et al.*, “A Trifunctional Electrolyte Enables Aqueous Zinc Ion Batteries with Long Cycling Performance,” *Adv. Funct. Mater.*, p. 2314388, Mar. 2024, doi: 10.1002/adfm.202314388.
[110] A.-S. Feiner and A. J. McEvoy, “The Nernst Equation,” *J. Chem. Educ.*, vol. 71, no. 6, p. 493, Jun. 1994, doi: 10.1021/ed071p493.
[111] Y. Kameda *et al.*, “Solvation Structure of Li^+ in Methanol and 2-Propanol Solutions Studied by ATR-IR and Neutron Diffraction with $^6Li/^7Li$ Isotopic Substitution Methods,” *J. Phys. Chem. B*, vol. 123, no. 23, pp. 4967–4975, Jun. 2019, doi: 10.1021/acs.jpcb.9b03477.
[112] Q. Ma *et al.*, “Regulation of Outer Solvation Shell Toward Superior Low-Temperature Aqueous Zinc-Ion Batteries,” *Adv. Mater.*, vol. 34, no. 49, p. 2207344, Dec. 2022, doi: 10.1002/adma.202207344.
[113] S. S. Munjewar, S. B. Thombre, and A. P. Patil, “Passive direct alcohol fuel cell using methanol and 2-propanol mixture as a fuel,” *Ionics*, vol. 25, no. 5, pp. 2231–2241, May 2019, doi: 10.1007/s11581-018-2627-y.
[114] C. Wang, K. Zhang, H. Xu, Y. Du, and M. C. Goh, “Anchoring gold nanoparticles on poly(3,4-ethylenedioxythiophene) (PEDOT) nanonet as three-dimensional electrocatalysts toward ethanol and 2-propanol oxidation,” *J. Colloid Interface Sci.*, vol. 541, pp. 258–268, Apr. 2019, doi: 10.1016/j.jcis.2019.01.055.
[115] R. Zhang *et al.*, “Weakly solvating aqueous-based electrolyte facilitated by a soft co-solvent for extreme temperature operations of zinc-ion batteries,” *Energy Environ. Sci.*, p. 10.1039.D4EE00942H, 2024, doi: 10.1039/D4EE00942H.
[116] Y.-C. Wu and Y.-C. Tai, “Effects of alcohol solvents on anatase TiO2 nanocrystals prepared by microwave-assisted solvothermal method,” *J. Nanoparticle Res.*, vol. 15, no. 6, p. 1686, Jun. 2013, doi: 10.1007/s11051-013-1686-2.
[117] J.-G. Park, S.-H. Lee, J.-S. Ryu, Y.-K. Hong, T.-G. Kim, and A. A. Busnaina, “Interfacial and Electrokinetic Characterization of IPA Solutions Related to Semiconductor Wafer Drying and Cleaning,” *J. Electrochem. Soc.*, vol. 153, no. 9, p. G811, 2006, doi: 10.1149/1.2214532.
[118] N. Sorour, W. Zhang, E. Ghali, and G. Houlachi, “A review of organic additives in zinc electrodeposition process (performance and evaluation),” *Hydrometallurgy*, vol. 171, pp. 320–332, Aug. 2017, doi: 10.1016/j.hydromet.2017.06.004.

[119] J. Ji *et al.*, “Zinc-Contained Alloy as a Robustly Adhered Interfacial Lattice Locking Layer for Planar and Stable Zinc Electrodeposition,” *Adv. Mater.*, vol. 35, no. 20, p. 2211961, May 2023, doi: 10.1002/adma.202211961.
[120] J. Zhang *et al.*, “Weakly Solvating Cyclic Ether Electrolyte for High-Voltage Lithium Metal Batteries,” *ACS Energy Lett.*, vol. 8, no. 4, pp. 1752–1761, Apr. 2023, doi: 10.1021/acsenergylett.3c00181.
[121] Y. Li, Z. Yu, J. Huang, Y. Wang, and Y. Xia, “Constructing Solid Electrolyte Interphase for Aqueous Zinc Batteries,” *Angew. Chem.*, vol. 135, no. 47, p. e202309957, Nov. 2023, doi: 10.1002/ange.202309957.
[122] D. Xie *et al.*, “ZnF $_2$ -Riched Inorganic/Organic Hybrid SEI: in situ-Chemical Construction and Performance-Improving Mechanism for Aqueous Zinc-ion Batteries,” *Angew. Chem. Int. Ed.*, vol. 62, no. 7, p. e202216934, Feb. 2023, doi: 10.1002/anie.202216934.
[123] Y. Wang *et al.*, “Manipulating Electric Double Layer Adsorption for Stable Solid-Electrolyte Interphase in 2.3 Ah Zn-Pouch Cells,” *Angew. Chem.*, vol. 135, no. 23, p. e202302583, Jun. 2023, doi: 10.1002/ange.202302583.
[124] G. Liang *et al.*, “Regulating Inorganic and Organic Components to Build Amorphous-ZnF $_x$ Enriched Solid-Electrolyte Interphase for Highly Reversible Zn Metal Chemistry,” *Adv. Mater.*, vol. 35, no. 20, p. 2210051, May 2023, doi: 10.1002/adma.202210051.
[125] Y. Li, X. Deng, J. Tian, Z. Liang, and H. Cui, “Ti3C2 MXene-derived Ti3C2/TiO2 nanoflowers for noble-metal-free photocatalytic overall water splitting,” *Appl. Mater. Today*, vol. 13, pp. 217–227, Dec. 2018, doi: 10.1016/j.apmt.2018.09.004.
[126] B. Li *et al.*, “A Review of Solid Electrolyte Interphase (SEI) and Dendrite Formation in Lithium Batteries,” *Electrochem. Energy Rev.*, vol. 6, no. 1, p. 7, Dec. 2023, doi: 10.1007/s41918-022-00147-5.
[127] R. P. Reji, S. K. C. Balaji, Y. Sivalingam, Y. Kawazoe, and S. Velappa Jayaraman, “First-Principles Density Functional Theory Calculations on the Potential of Sc $_2$ CO $_2$ MXene Nanosheets as a Dual-Mode Sensor for Detection of Volatile Organic Compounds in Exhaled Human Breath,” *ACS Appl. Nano Mater.*, vol. 6, no. 7, pp. 5345–5356, Apr. 2023, doi: 10.1021/acsanm.2c05474.
[128] Y. Li *et al.*, “Under-Water Superaerophobic Pine-Shaped Pt Nanoarray Electrode for Ultrahigh-Performance Hydrogen Evolution,” *Adv. Funct. Mater.*, vol. 25, no. 11, pp. 1737–1744, Mar. 2015, doi: 10.1002/adfm.201404250.
[129] O. Romiluyi, Y. Eatmon, R. Ni, B. P. Rand, and P. Clancy, “The efficacy of Lewis affinity scale metrics to represent solvent interactions with reagent salts in all-inorganic metal halide perovskite solutions,” *J. Mater. Chem. A*, vol. 9, no. 22, pp. 13087–13099, 2021, doi: 10.1039/D1TA03063A.